Article

Cell Host & Microbe

Intratumoral microbiota and host genotype cooperatively shape neutrophil cytotoxic functions in colorectal cancer

Graphical abstract

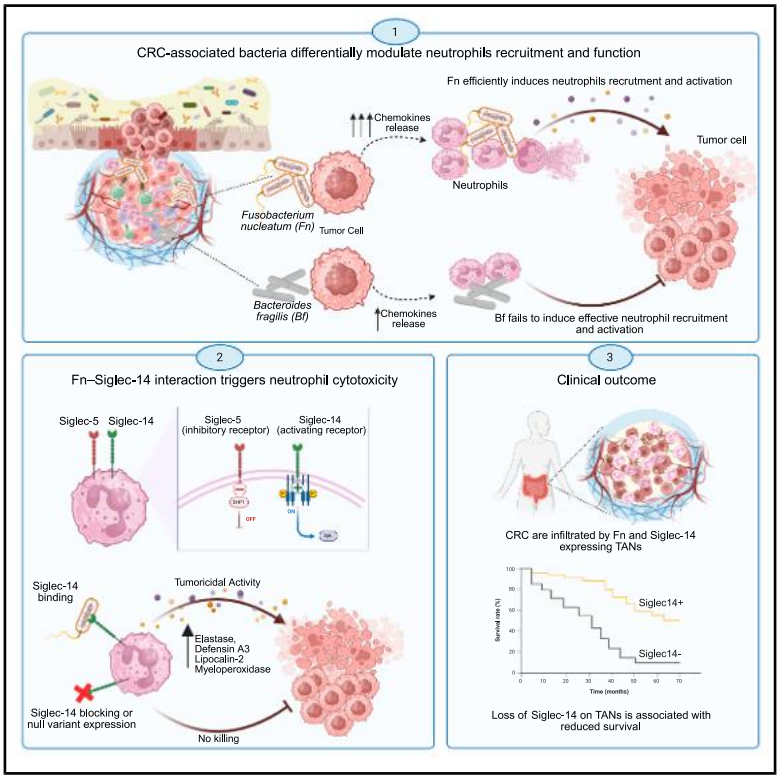

Highlights

- Intratumoral bacteria differentially promote neutrophil recruitment in CRC tissues
- *Fusobacterium nucleatum* (Fn) elicits neutrophil cytotoxicity via Siglec-14
- Expression of a Siglec-14 null variant prevents Fn-induced neutrophil cytotoxicity
- Neutrophil density, Fn load, and Siglec-14 expression predict survival in CRC

Authors

Elisa Sorrenti, Valeria Governa, Davide Bressan, ..., Giulio Cesare Spagnoli, Dimitrios Christoforidis, Giandomenica Iezzi

Correspondence

elisa.sorrenti@usi.ch (E.S.), giandomenica.iezzi@eoc.ch (G.I.)

In brief

Sorrenti et al. show that CRC-associated microbiota and host genetics regulate neutrophil function. *Fusobacterium nucleatum* (Fn) promotes neutrophil recruitment in tumors and triggers cytotoxic activity in a Siglec-14-dependent manner. High neutrophil density and Fn load predict better outcomes, whereas Siglec-14 loss associates with poorer survival, in CRC patients.

Sorrenti et al., 2026, Cell Host & Microbe *34*, 425–443
March 11, 2026
https://doi.org/10.1016/j.chom.2026.02.006

CellPress

Cell Host & Microbe

CellPress
OPEN ACCESS

Article

Intratumoral microbiota and host genotype cooperatively shape neutrophil cytotoxic functions in colorectal cancer

Elisa Sorrenti,[1,2,19,*] Valeria Governa,[3,19] Davide Bressan,[4] Eleonora Cremonesi,[3] Nicolò Formaggio,[5] Irene Latino,[2,6] Bianca Calì,[5] Cristina Torcasio,[7] Camilla Basso,[1,2] Jacopo Galafassi,[1,8] Martina Villa,[1,8] Carla Stornante,[9] Federica Cetti,[5] Diego Calabrese,[3] Caner Ercan,[10] Federica Mauri,[11] Laura Terzaghi,[1] Valentina Mele,[3] Elisa Poncioni,[9] Julija Djordjevic,[1,2] Agnese Cianfarani,[1,8] Mauro Tonolla,[11] Giuseppe Sconocchia,[12] Klaus-Peter Janssen,[13] Milo Frattini,[14] Jean-Philippe Theurillat,[5] Santiago F. Gonzalez,[2,6] Sara De Dosso,[2,15] Serenella Eppenberger-Castori,[10] Luigi Maria Terracciano,[16,17] Pietro Edoardo Majno-Hurst,[2,8] Fulvio Chiacchiera,[4] Lubor Borsig,[9] Giulio Cesare Spagnoli,[12] Dimitrios Christoforidis,[2,8,18] and Giandomenica Iezzi[1,2,8,20,*]

[1]Laboratory for Surgical Research, Institute for Translational Research Università della Svizzera Italiana (USI)-Ente Ospedaliero Cantonale (EOC), Bellinzona, Switzerland
[2]Faculty of Biomedical Sciences, USI, Lugano, Switzerland
[3]Department of Biomedicine, University of Basel, Basel, Switzerland
[4]Department of Cellular, Computational, and Integrative Biology, University of Trento, Povo, Trento, Italy
[5]Institute of Oncology Research (IOR), Bellinzona, Switzerland
[6]Institute for Research in Biomedicine (IRB), Bellinzona, Switzerland
[7]Nephrology Research Group, Institute for Translational Research USI-EOC, Bellinzona, Switzerland
[8]Department of Surgery, EOC, Lugano, Switzerland
[9]Institute of Physiology, University of Zürich, Zürich, Switzerland
[10]Institute of Pathology, Universitätsspital Basel, Basel, Switzerland
[11]Institute of Microbiology, University of Applied Sciences and Arts of Southern Switzerland (SUPSI), Bellinzona, Switzerland
[12]Institute of Translational Pharmacology, National Research Council, Rome, Italy
[13]Department of Surgery, School of Medicine, Klinikum rechts der Isar, Technical University of Munich (TUM), Munich, Germany
[14]Laboratory of Genetics and Molecular Pathology, Istituto Cantonale di Patologia EOC, Locarno, Switzerland
[15]Medical Oncology Department, Oncology Institute of Southern Switzerland (IOSI), EOC, Bellinzona, Switzerland
[16]Department of Biomedical Sciences, Humanitas University, Milan, Italy
[17]Pathology Unit, IRCCS Humanitas Research Hospital, Milan, Italy
[18]University of Lausanne, Lausanne, Switzerland
[19]These authors contributed equally
[20]Lead contact
*Correspondence: elisa.sorrenti@usi.ch (E.S.), giandomenica.iezzi@eoc.ch (G.I.)
https://doi.org/10.1016/j.chom.2026.02.006

SUMMARY

The role of tumor-associated neutrophils (TANs) infiltrating colorectal cancers (CRCs) is still debated. Here, we unravel that TAN recruitment and functions are modulated by intratumoral microbiota and only defined bacterial species can unleash neutrophil cytotoxic potential. *Fusobacterium nucleatum* promotes the production of neutrophil-recruiting chemokines by tumor cells and enhances neutrophil migration more efficiently than *Bacteroides fragilis.* Importantly, *Fusobacterium nucleatum*, but not *Bacteroides fragilis*, triggers neutrophils to release cytotoxic proteins showing tumoricidal activity *in vitro* and in xenograft models. Mechanistically, these effects are elicited upon *Fusobacterium nucleatum* binding to sialic-acid-binding immunoglobulin-like lectin (Siglec)-14 expressed by neutrophils but are impaired upon Siglec-14 blockade or loss-of-function polymorphisms. Supporting these findings, in human CRCs, elevated *Fusobacterium nucleatum* loads and high TAN densities correlate with improved prognosis, whereas lack of Siglec-14 expression is associated with reduced patient survival. Our findings identify microbiota composition and host genetic background as critical determinants of neutrophil functional profiles, offering insights into neutrophil-targeted therapeutic strategies in CRC.

INTRODUCTION

The tumor microenvironment (TME) plays a key role in colorectal cancer (CRC) development and progression.[1] Infiltration by defined populations of immune cells is widely known to be associated with clinical outcome. However, although high T cell density in tumor tissues has consistently been recognized to predict prolonged survival,[2,3] the clinical

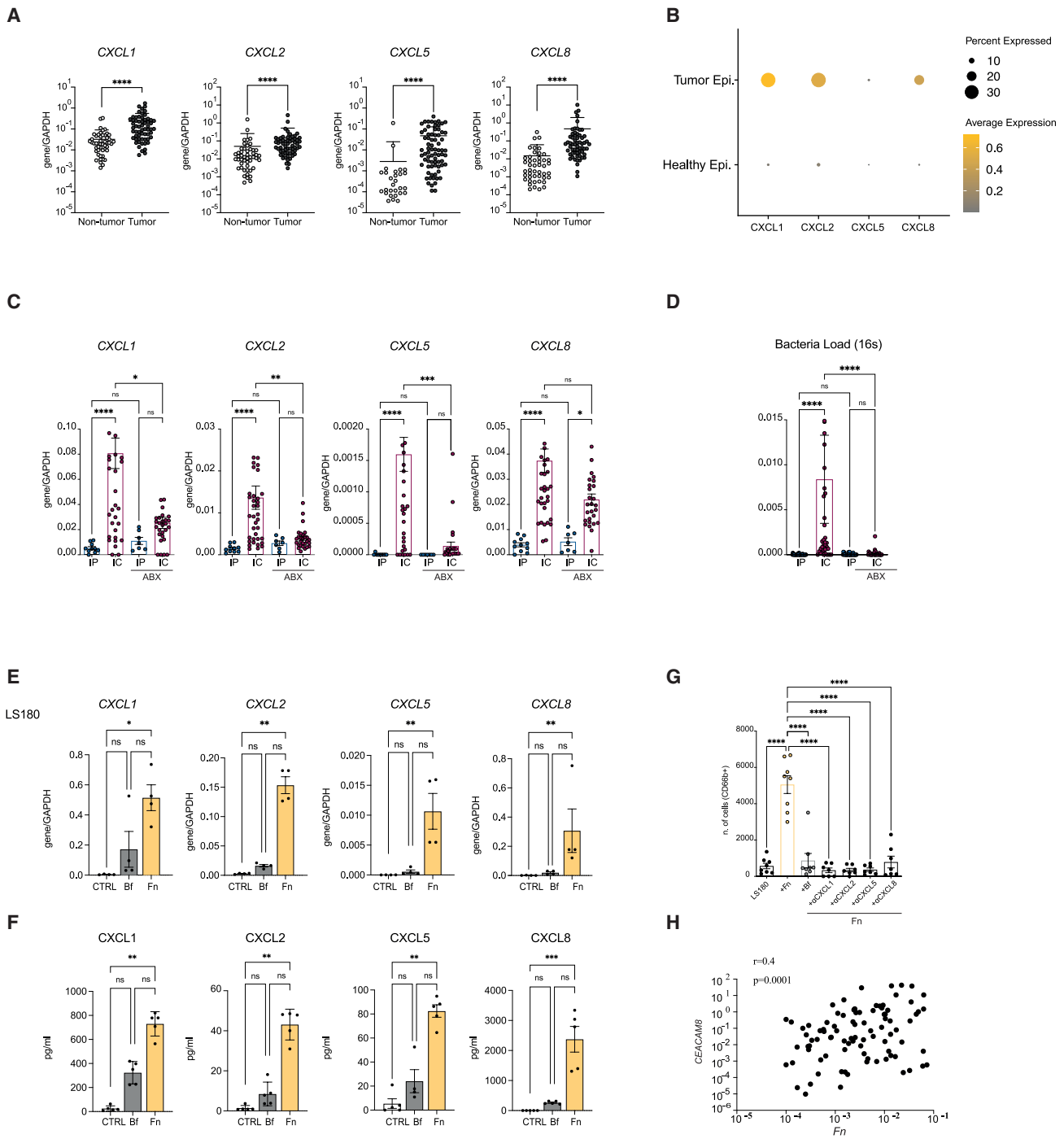

Figure 1. Gut bacterial species differentially promote the production of neutrophil-recruiting chemokines by CRC cells

(A) Expression of indicated chemokine genes was assessed by real-time PCR in a cohort of primary CRC tissues and matched adjacent non-tumoral tissues (cohort 1, $n = 61$, Table S1). Statistical significance was assessed by Wilcoxon test (****$p < 0.0001$).

(B) Expression of indicated chemokine genes was evaluated in a publicly available single-cell RNA-seq database.[40] Data refer to average expression levels and percentages of positive cells among tumoral ($n = 108,131$) and non-tumoral epithelial cells ($n = 60,164$).

(C and D) NSG mice were inoculated intra-cecum (i.c., $n = 17$) or intraperitoneal (i.p., $n = 66$) with human CRC cells (3×10^5 cells/mouse) from LS180 cell line. Following tumor development, starting from day 10, a randomized group of mice inoculated i.p. ($n = 7$) or i.c. ($n = 28$) were treated with ampicillin and vancomycin for 3 weeks (see Figure S1C). On day 31, xenografts were removed and expression levels of the indicated chemokine genes (C) and of the 16S gene (D) were analyzed by real-time PCR, using the GAPDH gene as reference. Cumulative data from three independent experiments are reported. Statistical significance was assessed by Kruskal-Wallis test (*$p < 0.05$, **$p < 0.01$, ***$p < 0.001$, ****$p < 0.0001$).

(legend continued on next page)

significance of tumor-associated neutrophils (TANs) is still debated.

Studies in experimental models suggest a pro-tumoral function of TANs through direct support of tumor development and spreading[4–7] or inhibition of T cell-mediated immune responses.[8,9] In contrast, studies investigating the prognostic significance of neutrophil infiltration in human CRC show contradictory results. Intriguingly, studies including Asian patient cohorts have mostly reported an association of neutrophil infiltration with reduced survival,[10–12] whereas those focusing on European or US patients consistently indicate that neutrophil infiltration correlates with favorable prognosis and responsiveness to chemotherapy in CRC,[13–18] possibly suggesting that genetic variants between patients from different ethnic groups or geographical areas may impact on TANs' clinical course.

The antitumor potential of neutrophils has recently been reported in other tumor types due to their ability to release cytotoxic factors,[19] boost antitumor T cell-mediated immune responses,[20,21] and successfully synergize with immunological checkpoint inhibitors (ICIs) in cancer treatment.[22–24] However, the stimuli that elicit the antitumor functions of neutrophils remain unclear.[25]

CRC arises in a microenvironment heavily populated by bacteria of gut microbiota. Increased mucosal permeability, already detectable in early precancerous conditions, favors bacterial translocation into the submucosa[4] and direct interaction with immune cells. The impact of the gut microbiota on CRC has been explored in detail,[26,27] and the presence of defined bacterial species, such as *Fusobacterium nucleatum,* in stools and tumor tissues has been shown to promote cancer cell proliferation and immune evasion.[28–32] A modest but significant association between *Fusobacterium nucleatum* abundance in CRC tissues and unfavorable tumor prognosis has also been reported.[33–35] Yet, intriguingly, *Fusobacterium nucleatum* and other CRC-infiltrating bacteria were found to trigger in tumor cells the production of a large spectrum of chemokines, including those promoting neutrophil recruitment.[36–38]

Neutrophils represent a first-line defense against bacteria,[39] and spatial transcriptomics analysis has recently unraveled their presence within tumor areas heavily colonized by CRC-infiltrating bacteria.[38] However, the functional outcome and prognostic relevance of these interactions have not been thoroughly investigated.

To address these issues, in this study we investigated the impact of the most abundant CRC-associated bacteria on neutrophil recruitment and functional modulation.

RESULTS

Expression and clinical relevance of neutrophil-recruiting chemokine genes in CRC

We initially investigated the expression of genes encoding neutrophil-recruiting chemokines, including *CXCL1*, *CXCL2*, *CXCL5*, and *CXCL8*, in human CRC tissues (Tables S1 and S2). The expression of these genes, as assessed by quantitative PCR using specific probes, was significantly higher in tumor than in corresponding adjacent non-tumoral tissues (cohort 1, $n = 61$, Figure 1A; Table S1). Moreover, data from single-cell RNA sequencing (scRNA-seq) databases[40] indicated that this difference is particularly evident within the epithelial compartment (Figure 1B), thus suggesting that tumor cells may represent a major source of neutrophil-recruiting chemokines. In CRC tissues (cohort 2, $n = 145$, Table S2), the expression of genes encoding neutrophil-recruiting chemokines significantly correlated with neutrophil infiltration, as indicated by the expression of *CEACAM8*, encoding the neutrophil marker CD66b (Figure S1A). Furthermore, in The Cancer Genome Atlas (TCGA) database, it was associated with prolonged survival (Figure S1B).

Neutrophil-recruiting chemokine production by CRC cells is enhanced upon interaction with gut microbiota

To evaluate the impact of CRC-infiltrating bacteria on the production of neutrophil-recruiting chemokines by tumor cells, we took advantage of a transplantable CRC model based on intracecal (i.c.) or intraperitoneal (i.p.) injection of human CRC cells into immunodeficient non-obese diabetic-severe combined immunodeficiency-gamma (NSG) mice (Cremonesi et al.[36] and Mele et al.[41]; Figure S1C). We observed a significantly higher expression of neutrophil-recruiting chemokine genes in i.c. tumors, exposed to the gut microbiota, compared with virtually sterile i.p. tumors (Figure 1C), showing negligible bacterial load (Figure 1D). Antibiotic treatment abolished this difference, thus indicating that the bacterial component was indeed the main factor responsible for this effect (Figures 1C and 1D).

Gut bacterial species promote the production of neutrophil-recruiting chemokines by CRC cells

We next investigated the effects mediated by the two most abundant bacterial species in human CRC tissues, i.e., *Fusobacterium nucleatum* and *Bacteroides fragilis*, as detected in a previously analyzed cohort[36] as well as in a publicly available human CRC database (Sepich-Poore et al.[42]; Figures S1D and S1E). Exposure of human CRC cell lines to these bacteria boosted chemokine

(E and F) CRC cells from LS180 cell line (3.5×10^5/mL) were incubated with control (CTRL) medium or live*Fusobacterium nucleatum* or *Bacteroides fragilis* (bacteria: CRC cell ratio = 50:1). Fn, *Fusobacterium nucleatum*; Bf, *Bacteroides fragilis*. (E) Expression of indicated chemokine genes in tumor cells was assessed after 4 h by real-time PCR. Cumulative data from 4 independent experiments are reported. Individual dots represent average levels from 3 replicates. Statistical significance was assessed by Kruskal-Wallis test (*$p < 0.05$, **$p < 0.01$). (F) Release of the indicated chemokines was measured by specific ELISA assays after overnight culture. Cumulative data from 5 independent experiments are shown. Individual dots represent average levels from 3 replicates. Statistical significance was assessed by Kruskal-Wallis test (*$p < 0.05$, **$p < 0.01$, ***$p < 0.001$).

(G) PBN migration toward culture supernatants from *Fusobacterium nucleatum*- or *Bacteroides fragilis*-stimulated LS180 cells was tested in transwell plates (5 μm pore size, 1.5×10^5 PBNs/well), in the presence or absence of the indicated chemokine-specific antibodies. Numbers of PBNs migrated into lower chambers were quantified after 2 h by CyQUANT Cell Proliferation Assay Kit. Cumulative data from 5 independent experiments are shown. Statistical significance was assessed by Tukey's multiple comparison test (****$p < 0.0001$).

(H) Correlation between expression of CEACAM8 gene and *Fusobacterium nucleatum* loads in human primary CRC samples (cohort 2, $n = 145$, Table S2) as assessed by real-time PCR by using specific probes (see key resources table). Spearman r coefficients and p values are indicated.

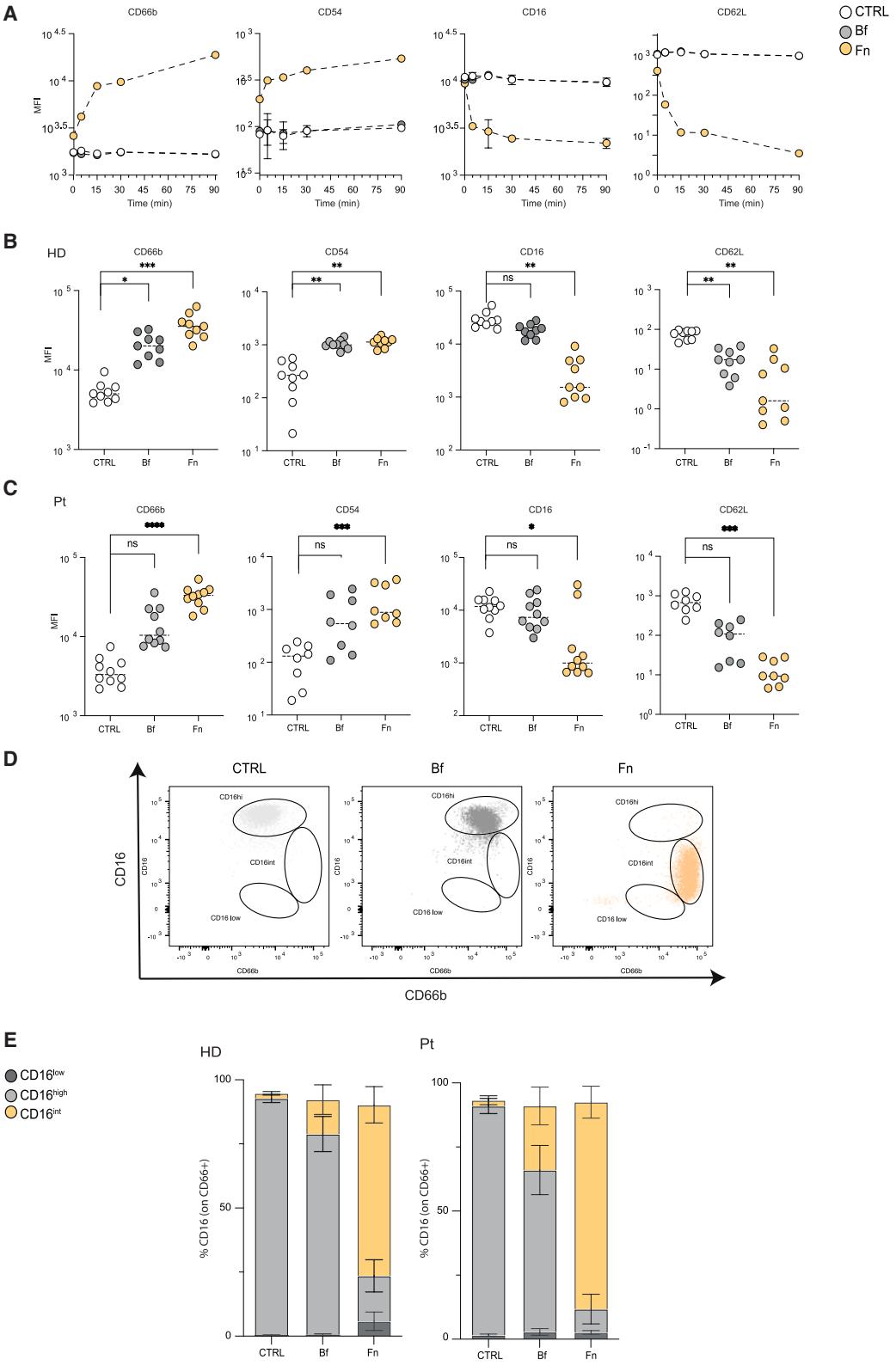

(legend on next page)

expression at both gene and protein levels (Figures 1E, 1F, S1F, and S1G). However, only *Fusobacterium nucleatum*-induced chemokine gene expression and protein release to significantly higher levels than controls. Consistently, supernatants from *Fusobacterium nucleatum*-stimulated tumor cells promoted chemokine-dependent neutrophil migration *in vitro* more efficiently than those from *Bacteroides fragilis*-stimulated CRC cells (Figures 1G and S1H). Comparable bacteria-mediated effects on chemokine gene expression were also observed in murine MC38 and CT26 CRC cell lines *in vitro* (Figures S2A and S2B). Furthermore, in immunocompetent mice bearing i.c. xenografts, gut colonization with *Fusobacterium nucleatum* led to increased expression of the *CXCL1* gene in both MC38 and CT26 tumors and of the *CXCL5* gene in MC38 tumors. In contrast, colonization with *Bacteroides fragilis* induced *CXCL1* expression only in MC38 but not in CT26 tumors. Importantly, *Fusobacterium nucleatum*, but not *Bacteroides fragilis*, colonization resulted in increased TAN densities (Figures S2F and S2G). In line with these findings, in human primary CRC tissues, *Fusobacterium nucleatum* abundance was associated with neutrophil infiltration (cohort 2, Figure 1H).

CRC-associated bacteria differentially trigger neutrophil activation

We then evaluated the outcome of direct bacteria-neutrophil interaction. Exposure of peripheral blood neutrophils (PBNs) from healthy donors (HDs) to *Fusobacterium nucleatum* resulted in strong activation, as indicated by CD66b and CD54 marker upregulation and concomitant CD16 and CD62L downregulation (Figures 2A and 2B), as detected by flow cytometry. This phenotypic modulation was detectable as early as 5 min after exposure and reached a plateau after approximately 3 h of stimulation (Figures 2A, 2B, and S3A–S3C). In contrast, a phenotypic modulation of a lesser magnitude was detectable in *Bacteroides fragilis*-stimulated neutrophils (Figures 2A, 2B, and S3A–S3C). Comparable results were observed in PBNs from patients with CRC (cohort 3, Table S3; Figure 2C).

Based on CD66b and CD16 expression levels, as detectable in PBNs from HD as well as from patients with CRC, we could identify three main neutrophil subpopulations: $CD66b^{int}$ $CD16^{high}$, referred to as $CD16^{high}$, mostly prevalent in non-stimulated and *Bacteroides fragilis*-exposed PBNs; $CD66b^{high}CD16^{int}$, referred to as $CD16^{int}$, mostly abundant in *Fusobacterium nucleatum*-exposed PBNs, and $CD66b^{int}CD16^{low}$, referred to as $CD16^{low}$, including minor PBN fractions in all experimental conditions (Figures 2D and 2E).

Live cell-imaging of bacteria-activated human PBNs (Videos S1, S2, S3, and S4) further demonstrated that, unlike PBNs undergoing phorbol 12-myristate 13-acetate (PMA) stimulation (Video S2), *Fusobacterium nucleatum*-activated PBNs remained viable over time and exhibited increased motility and cluster formation (Video S4; Figure S3D). Interestingly, PBNs formed stable clusters in response to *Fusobacterium nucleatum* incubation and were characterized by the release of multiple intracytoplasmic DNA-containing vesicles (Figure S3D), possibly suggesting the occurrence of vital NETosis.[43] In contrast, the behavior and morphology of *Bacteroides fragilis*-exposed PBNs (Video S3; Figure S3D) did not significantly differ from those of unstimulated PBNs (Video S1; Figure S3D).

Distinct secretomes are detected upon neutrophil interaction with different bacterial species

Proteomic analysis of neutrophil-conditioned media after bacterial stimulation revealed differential secretion of several soluble factors. In particular, upon *Fusobacterium nucleatum*—but not *Bacteroides fragilis*—exposure, a panel of seven proteins, including elastase, defensin A3, lipocalin-2, myeloperoxidase, matrix metalloproteinases (MPPs) 8 and 9, and cathelicidin (Figure 3A; Table S4) were released, consistent with the activation of defense responses, including degranulation, and cytotoxic pathways (Figure 3B). In contrast, exposure to *Bacteroides fragilis* appeared to inhibit the release of several proteins, including CFL1, CUTA, TMSB4X, HIST1H1C, IGFBP2, APOC3, and FKBP12-Exin.

Cytotoxic functions of human neutrophils are elicited upon exposure to *Fusobacterium nucleatum* but not *Bacteroides fragilis*

Because enzymes produced by activated human neutrophils were previously shown to be endowed with cytotoxic activity,[19] we then tested the cytotoxic potential of *Fusobacterium nucleatum*-activated PBNs. Remarkably, neutrophil-conditioned media following *Fusobacterium nucleatum*, but not *Bacteroides fragilis*, stimulation from HD and patients with CRC showed tumoricidal activity on CRC cells *in vitro* (Figures 3C–3E, S3E, and S3F).

To test the cytotoxic potential of bacteria-activated neutrophils *in vivo*, we first evaluated the reactivity of murine neutrophils to CRC-associated bacteria *in vitro*. Upon stimulation with *Fusobacterium nucleatum*, but not *Bacteroides fragilis*, murine neutrophils underwent phenotypic modulation, characterized by upregulation of Ly6G, CD54, CD18, and, unlike human neutrophils, CD62L as well, (Figures S4A and S4B). However, unexpectedly, we did not detect any significant cytotoxic activity in tumor cells (Figures S4C and S4D). Consistently, in mice bearing orthotopic xenografts, colonization with *Fusobacterium*

Figure 2. CRC-associated bacteria differentially induce neutrophil activation

PBNs (5×10^5 in 1 mL) from healthy donors (HDs) and patients with CRC (Pt) from cohort 3 (Table S5) were incubated with CTRL medium, live *Fusobacterium nucleatum*, or *Bacteroides fragilis* (bacteria: neutrophil ratio 50:1) at 37°C. At different time points, expression levels of the indicated surface markers were analyzed by flow cytometry upon staining with specific antibodies (see key resources table). Fn, *Fusobacterium nucleatum*; Bf, *Bacteroides fragilis*.

(A) Expression kinetics of indicated markers in untreated or bacteria-stimulated PBNs from HD ($n = 3$). Average levels of mean fluorescence intensity (MFI) ± SD are reported.

(B and C) MFI of indicated markers in untreated or bacteria-stimulated PBNs from HD (B, $n = 9$) and Pt (C, $n = 10$) after 3 h of stimulation. Each dot represents the average of 3 replicates from individual donors. Statistical significance was assessed by Friedman test (*$p < 0.05$, **$p < 0.01$, ***$p < 0.001$; ****$p < 0.0001$).

(D) Representative dot plots illustrating PBN subsets identified based on CD16 and CD66b expression levels under the different stimulatory conditions.

(E) Percentages (average ± SD) of PBN subsets detected under the different stimulatory conditions in PBNs from HD ($n = 9$) and Pt ($n = 10$).

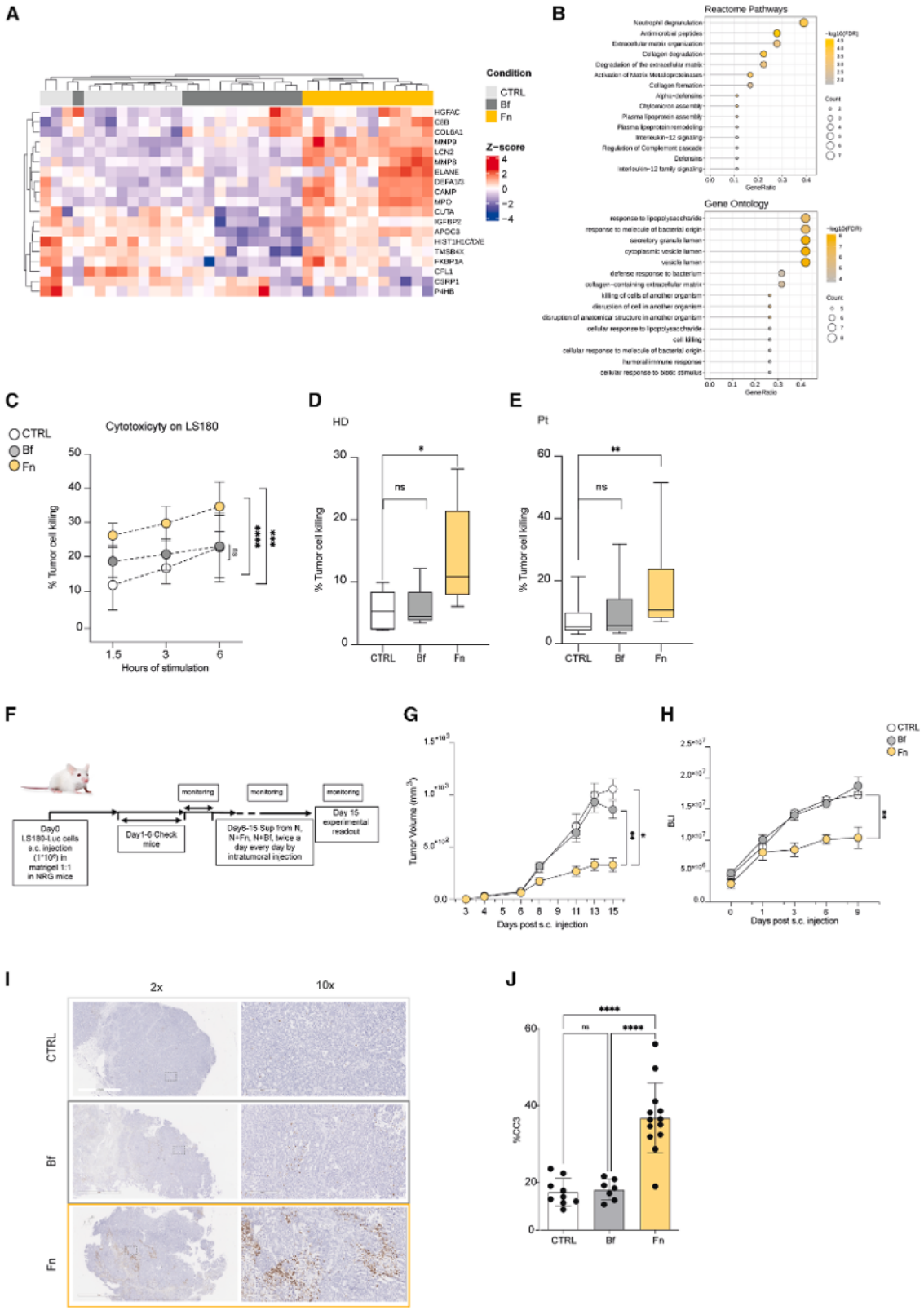

Figure 3. *Fusobacterium nucleatum*, but not *Bacteroides fragilis*, triggers neutrophil cytotoxic functions

Neutrophil-conditioned media collected from HD following 3 h of bacteria stimulation was evaluated by proteomic analysis. Differentially released proteins were identified upon ANOVA multiple sample test (false discovery rate [FDR] < 0.05, see Table S4). Fn, *Fusobacterium nucleatum*; Bf, *Bacteroides fragilis*.

(legend continued on next page)

nucleatum or *Bacteroides fragilis* did not lead to any significant effect on tumor growth (Figures S4E and S4F).

Therefore, to provide *in vivo* validation of our findings, we tested the effects of human neutrophil-conditioned media after bacterial stimulation on the growth of CRC xenografts, generated by subcutaneous (s.c.) injection of human CRC cells in immunodeficient non-obese diabetic (NOD)-Rag1 and IL2 receptor gamma-chain-deficient (NRG) mice (Figure 3F). Intratumoral injection of neutrophil-conditioned media following *Fusobacterium nucleatum* stimulation resulted in significant tumor growth inhibition and increased tumor cell death. In contrast, injection of neutrophil-conditioned media following *Bacteroides fragilis* stimulation failed to induce any significant effect (Figures 3G–3L). Thus, CRC-associated bacteria differ in their capacity to trigger neutrophils' cytotoxic functions.

Bacteria-mediated neutrophil activation is induced upon engagement of Siglec-14

Next, we investigated mechanisms mediating bacteria-neutrophil interaction resulting in the elicitation of cytotoxic effects. Binding of fluorescence-labeled *Fusobacterium nucleatum* was detectable in up to 25% of neutrophils following 5 min of stimulation and decreased over time, possibly suggesting bacterial internalization. In contrast, *Bacteroides fragilis* binding was only marginally detected (Figures 4A and 4B).

Human neutrophils express different surface receptors potentially binding bacterial determinants, including Toll-like receptor 2 (TLR2), TLR4, and the paired sialic-acid-binding immunoglobulin-like lectin (Siglec)-5 and -14.[44,45] We therefore assessed bacteria-induced neutrophil activation in the presence of blocking antibodies targeting TLR2, TLR4, and both Siglec-5 and -14. Indeed, due to the high homology of their extracellular domains, currently available blocking antibodies are unable to discriminate between these two Siglec receptors. Blocking of TLR4, but not of TLR2 or Siglec-5/14, completely inhibited *Fusobacterium nucleatum*-mediated phenotypic modulation (Figure 4C). However, it did not significantly affect neutrophil tumor-killing capacity (Figure 4D). In contrast, cytotoxicity was completely abolished upon Siglec-5/14 blockade (Figure 4D), thus indicating that Siglec-5/14 engagement is essential for the elicitation of *Fusobacterium nucleatum*-induced neutrophil cytotoxic functions. As expected, simultaneous TLR4 and Siglec-5/14 blocking abrogated both *Fusobacterium nucleatum*-mediated neutrophil phenotypic modulation and elicitation of cytotoxic activity (Figures S5A and S5B).

Expression of Siglec-5/14 was clearly detectable on PBNs and was slightly downmodulated upon exposure to *Fusobacterium nucleatum* and, to a lower extent, to *Bacteroides fragilis* (Figures S5C and S5D). Confocal imaging demonstrated colocalization of Siglec-5/14 with *Fusobacterium nucleatum* but not with *Bacteroides fragilis* (Figure 4E). Notably, although in unstimulated and *Bacteroides fragilis*-exposed neutrophils Siglec-5/14 appeared to be localized only at the cell membrane level, in *Fusobacterium nucleatum*-stimulated neutrophils both membrane and cytoplasmic localization were detected, suggesting internalization of the receptor upon *Fusobacterium nucleatum* binding (Figures 4E and 4F). Consistently, transmission electron microscopy (TEM) imaging confirmed *Fusobacterium nucleatum*, but not *Bacteroides fragilis*, internalization, which was inhibited upon Siglec-5/14, but not TLR4, blocking (Figure 4G).

To further investigate the molecular determinants mediating the interaction between *Fusobacterium nucleatum* and Siglec-5 and -14, we evaluated the binding capacity of soluble Siglec-5 and Siglec-14-Fc chimeras to *Fusobacterium nucleatum*-derived LPS (Figures S5E and S5F). Strikingly, Siglec-14 bound efficiently to *Fusobacterium nucleatum*-LPS, whereas Siglec-5 exhibited minimal binding (Figure 4H).

Extent of bacteria-mediated neutrophil activation correlates with Siglec-14 genotype

Notably, Siglec-5 and -14 differ in their signaling pathways. Like most Siglecs, Siglec-5 contains an immunoreceptor-tyrosine inhibitory motif (ITIM), thereby mediating inhibitory signals. In contrast, Siglec-14 has no tyrosine regulatory motifs but can deliver an activating signal upon association with theDNAX-activating protein of 12 kD (DAP12) coreceptor, containing an immunoreceptor-tyrosine activation motif (ITAM).[46]

Thus, to further demonstrate the specific involvement of Siglec-14 in *Fusobacterium nucleatum*-induced neutrophil cytotoxic effects, we tested responsiveness to *Fusobacterium nucleatum* of neutrophils isolated from donors harboring different genotypes at the Siglec-14 locus (Figures S5G and S5H). Indeed, a common

(A) Unsupervised hierarchical analysis of *Z* score values of label-free quantification intensity (LFQI).
(B) The impact of identified proteins on defined biological pathways was evaluated upon analysis of Reactome pathways and Gene Ontology (GO) databases. Size of depicted dots is proportional to the number of proteins involved in the indicated pathways. Colors indicate FDR values.
(C–E) PBNs from healthy donors (HDs, $n = 9$) or patients with CRC (Pt, $n = 10$, cohort 3, Table S3) were stimulated as described in Figure 2. At the indicated time points, supernatants were collected and, following high-speed centrifugation and filtering at 0.2 μm to remove potential residual bacteria, were incubated with LS180 cells. After 24 h, tumor cell viability was assessed by flow cytometry following annexin-V and LIVE/DEAD staining. (C) Percentages of tumor cell killing upon incubation of tumor cells with supernatants collected at the indicated time points from untreated or bacteria-stimulated PBNs from HD ($n = 9$). Average ± SD are shown. (D and E) Percentages of tumor cell killing upon incubation of tumor cells with supernatants collected from PBNs of HD (D) or Pt (E) after 3 h of stimulation. Statistical significance was assessed by Friedman test (*$p < 0.05$, **$p < 0.01$).
(F) Experimental scheme used for *in vivo* experiments. Luciferase-expressing LS180 cells (Luc-LS180) were injected s.c. in NRG mice (10^6 cells/mouse). Upon tumor development, starting from day 6, supernatants from untreated (CTRL), *Bacteroides fragilis*- or *Fusobacterium nucleatum*- stimulated PBNs were injected intratumorally (100 μL) twice daily (10–13 mice/group).
(G and H) Tumor growth was monitored over time by assessing tumor volumes by caliper (G) and bioluminescence intensity (BLI, H). Statistical significance was assessed by Tukey's multiple comparison test (*$p < 0.05$; **$p < 0.01$).
(I and J) On day 15, tumors were harvested from surviving mice and tumor cell death in tissue was evaluated by cleaved-caspase-3 (CC3) staining. (I) Representative CC3 staining in tumors treated with supernatants from different PBN cultures. (J) Cumulative percentages of $CC3^+$ cells detected in all tumors treated with supernatants from different PBN cultures. Each dot represents average from regions of interest (ROIs) detected in individual tumors ($n = 6$ ROI/tumor). Columns indicate average in each experimental group. SD are indicated by bars.
Statistical significance was assessed by Tukey's multiple comparison test (****$p < 0.0001$).

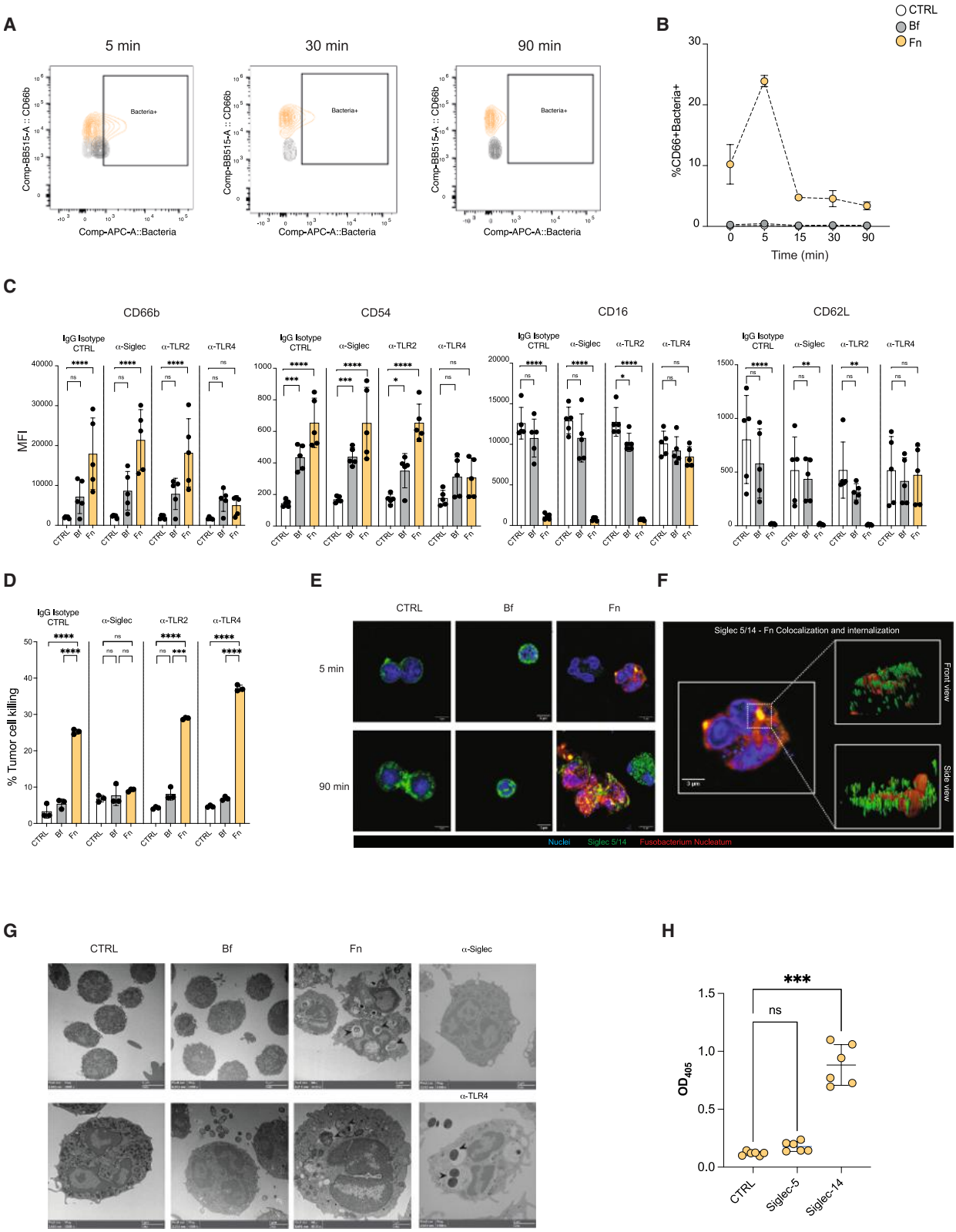

(legend on next page)

genetic polymorphism has previously been described, implying a fusion between Siglec-5 and Siglec-14 loci, resulting in the functional deletion of Siglec-14.[47]

Neutrophils from Siglec-14 null HD showed a phenotypic modulation upon co-culture with *Fusobacterium nucleatum* comparable to that detectable in cells from wild-type (WT) or heterozygous (WT/null) donors (Figure S5I). Most strikingly, however, they failed to display tumor-killing activity (Figure 5A). Accordingly, in all PBNs tested, the extent of cytotoxic activity correlated with Siglec-14 genotype, being higher in WT and progressively decreasing in WT/null and null individuals (Figure 5B). Activation of DAP12 signaling pathways, involving mitogen-activated protein kinase (MAPK) family, as indicated by phospho-p38 and pERK, was detected in *Fusobacterium nucleatum*-stimulated neutrophils from Siglec-14 WT but not Siglec-14 null donors (Figure 5C). Furthermore, in myeloid cell lines transduced with Siglec-14, but not in those transduced with Siglec-5, a higher phosphorylation of spleen tyrosine kinase (SYK) following *Fusobacterium nucleatum* stimulation was evident (Figures S5J and S5K). Altogether, these data support the engagement of Siglec-14 and its activating pathway in *Fusobacterium nucleatum*-induced neutrophil cytotoxic functions.

Engagement of Siglec-14 triggers distinct activating signatures in *Fusobacterium nucleatum*-stimulated neutrophils

To investigate in greater detail signaling pathways and transcriptional programs activated downstream of Siglec-14, we evaluated the transcriptional profiles of *Fusobacterium nucleatum*- or *Bacteroides fragilis*-stimulated neutrophils from Siglec-14 WT or null donors at the single-cell level. Three major clusters corresponding to untreated (cluster 1), *Bacteroides fragilis*- (cluster 2), and *Fusobacterium nucleatum*-stimulated neutrophils (cluster 3) were detectable (Figure 5D). Upon differential expression analysis, most expressed genes in each cluster were identified (Figure 5E). Untreated neutrophils showed overexpression of baseline housekeeping and cytoskeletal regulators (*ARHGAP25* and *RHOB*) and of negative regulators of nuclear factor κB (NF-κB) (*LRRC25*) and MAPK (*DUSP6*) pathways, consistent with their resting state. In contrast, these pathways were downregulated in *Bacteroides fragilis*-exposed and completely suppressed in *Fusobacterium nucleatum*-exposed neutrophils, whereas the concomitant upregulation of cytokine- and chemokine-related genes (*IL1B*, *CCL3*, *CCL4*, *CCL4L2*, and *CCL3L3*) was detectable, indicating the activation of a canonical inflammatory response. However, in *Bacteroides fragilis*-stimulated neutrophils, genes associated with regulatory feedback (*ZC3H12A*, *TNFAIP3*, *NFKBID*, and *NFKBIZ*) were also upregulated, suggesting the engagement of negative-control mechanisms. In contrast, *Fusobacterium nucleatum*-exposed neutrophils displayed lower expression of negative regulators but overexpression of MAPK/ERK pathway activation (*BRAF*, *MAPK6*, *ETS2*, and *NR4A3*), NF-κB pathway engagement (*IRAK2* and *NFKB1*), and genes related to cytoskeletal remodeling and motility (*DOCK4* and *FGD4*), thus reflecting a transition toward a fully transcriptionally active and migratory inflammatory phenotype (Figure 5E).

Transcriptional profiles of Siglec-14 WT and null neutrophils within each cluster could be further discriminated (Figure 5F). In cluster 3 (*Fusobacterium nucleatum*-stimulated neutrophils), 243 genes differentially expressed between WT and null neutrophils were identified (see Table S6), mostly related to cytokine-mediated signaling, positive regulation of NF-κB and MAPK cascade, and neutrophil migration (Figure 5G). These additional data demonstrate that Siglec-14 is a key mediator of the signaling pathways activated in neutrophils in response to *Fusobacterium nucleatum* stimulation.

CRC-derived TANs express Siglec-14 and show evidence of bacteria-induced activation

Altogether, the above-described findings indicate that Siglec-14 engagement by *Fusobacterium nucleatum* results in the elicitation of neutrophil-mediated cytotoxic functions. To verify that similar interaction and activation also occur within CRC tissues, we investigated the phenotypes of CRC-TANs in freshly excised clinical specimens of tumor and matched non-tumor colonic tissues (cohort 3, $n = 34$, Table S3) by large-scale flow cytometry. Neutrophils were detected within the myeloid cell fraction and in most samples appeared to be enriched in tumors compared with non-tumor tissues (Figures 6A, S6A, and S6B). TANs displayed high expression of CD66b, as previously observed,[16] and heterogeneous expression of CD16 and CD54 markers.

Figure 4. *Fusobacterium nucleatum*-mediated neutrophil activation is induced upon engagement of Siglec-14

(A and B) PBNs from HD were incubated with *Bacteroides fragilis* or *Fusobacterium nucleatum*, labeled with DID fluorescent dye. At the indicated time points, binding of bacteria to PBNs and expression of Siglec-5/14 was assessed by flow cytometry. (A) Representative dot plot showing acquisition of fluorescence by PBNs upon exposure to labeled bacteria. (B) Percentages of bacteria$^+$ PBNs detected over time. Average ± SD of triplicate cultures are shown.

(C and D) PBNs from HD were stimulated with *Bacteroides fragilis* or *Fusobacterium nucleatum* in the presence of blocking antibodies specific for TLR2 (10 μg/mL), TLR4 (20 μM), Siglec-5/14 (10 μg/mL), or with immunoglobulin G (IgG) isotype CTRL. After 1.5 h, neutrophil phenotypic modulation and cytotoxic activity of neutrophil-conditioned media post-bacteria stimulation were assessed. (C) MFI of indicated markers in untreated or bacteria-stimulated PBNs under the different experimental conditions. Each dot represents the average of duplicates from individual donors ($n = 5$). (D) Percentages of tumor cell killing upon incubation of LS180 cells with neutrophil-conditioned media following bacteria stimulation. Statistical significance was assessed by Tukey's multiple comparison test (*$p < 0.05$, **$p < 0.01$, ***$p < 0.001$; ****$p < 0.0001$).

(E and F) PBNs were stimulated with labeled bacteria (red), as detailed above. At the indicated time points, confocal imaging was performed upon staining with DAPI (blue) and anti-Siglec-5/14 (green). Representative pictures at 63× magnification are shown. (F) Enlarged view of *Fusobacterium nucleatum*-stimulated PBNs after 5 min. *Fusobacterium nucleatum* colocalization with Siglec-5/14 (front view) and internalization (side view) is detectable.

(G) Bacteria-stimulated PBNs untreated or exposed to *Bacteroides fragilis* or *Fusobacterium nucleatum*, in the absence or presence of anti-TLR4 or anti-Siglec5/14 blocking antibodies, were harvested after 1.5 h stimulation and TEM imaging was performed. Pictures taken at low (2,000–3,400×, upper) and high magnification (4,300–8,500×, lower) are shown. Arrows indicate internalized bacteria. Fn, *Fusobacterium nucleatum*; Bf, *Bacteroides fragilis*.

(H) Binding of soluble Siglec-5-Fc and Siglec-14-Fc chimeras, pre-complexed with AP-conjugated goat-anti-human IgG antibodies, was evaluated by ELISA. Following development with p-nitrophenyl phosphate (pNPP), absorbance at 405 nm wavelength was measured. Optical density (OD) values from six replicates from two independent experiments are reported. Statistical significance was assessed by Kruskal-Wallis test (***$p < 0.001$).

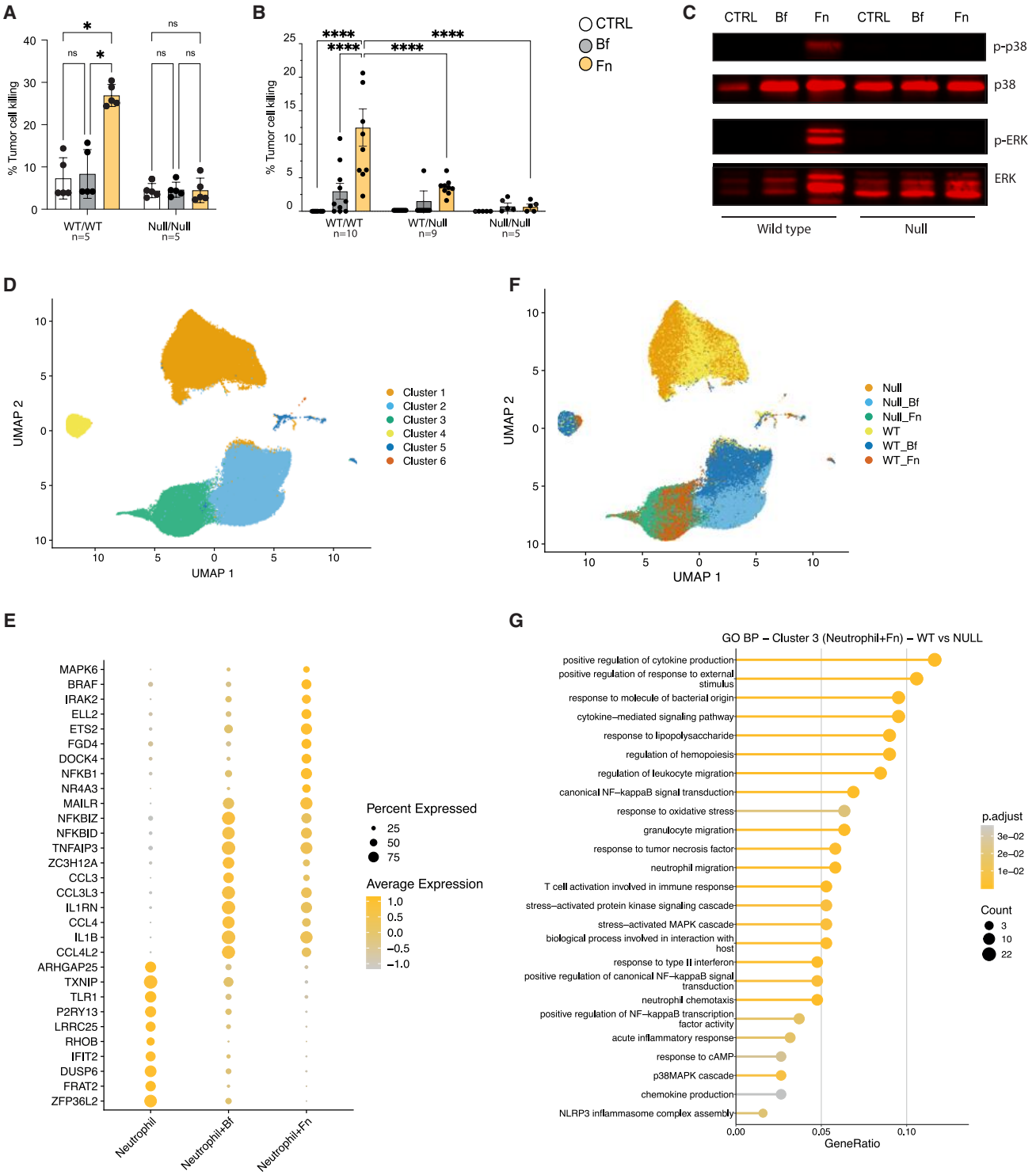

Figure 5. Engagement of Siglec-14 triggers distinct activating signatures in *Fusobacterium nucleatum*-stimulated neutrophils

(A) PBNs from HD carrying WT alleles (WT/WT, $n = 5$), or homozygous loss-of-function polymorphism at Siglec-5/14 locus[47] (null/null, $n = 5$), were stimulated with *Bacteroides fragilis* or *Fusobacterium nucleatum*, as detailed above. After 3 h, culture supernatants were collected, and their tumor cell killing ability was assessed on LS180 cells, as detailed above. Each dot represents average of triplicate cultures from individual donors. Average among donors is indicated by columns; SD is indicated by bars. Statistical significance was assessed by Tukey's multiple comparison test (*$p < 0.05$).

(legend continued on next page)

Interestingly, expression levels of CD54 and CD16 appeared to be inversely modulated, similar to the phenotypes of *in vitro Fusobacterium nucleatum*-stimulated PBNs (Figure 6B). Moreover, the three main neutrophil subtypes identified in bacteria-stimulated PBNs, based on CD16 levels, were also clearly detectable in TANs, with the CD16^{int} subset representing the most prevalent phenotype, consistent with bacteria-induced activation (Figures 6C and 6D). Notably, percentages of CD16^{int} TANs significantly correlated with those of *Fusobacterium nucleatum*-stimulated autologous PBNs (Figure S6C).

RNAscope and immunohistochemical (IHC) staining confirmed CRC infiltration by *Fusobacterium nucleatum* and TANs, respectively (Figures 6E and S6D). Siglec-14 was expressed in a large fraction of CRC-derived TANs, as assessed by flow cytometry (Figures 6F, 6G, and S6B) and confocal imaging (Figure 6H). Strikingly, TEM imaging of Siglec-14-expressing TANs revealed a morphology resembling that of *Fusobacterium nucleatum*-activated PBNs, with evidence of bacterial internalization (Figures 6H and 6I).

Furthermore, analysis of a publicly available scRNA-seq database of human primary CRCs[40] confirmed activation of MAPK and NF-κB cascades among the most upregulated signaling pathways in CRC-associated TANs (Figure 6J), consistent with the identified transcriptomic profiles of *Fusobacterium nucleatum*-stimulated neutrophils.

To verify the clinical impact of *Fusobacterium nucleatum*-TAN interactions occurring within CRC tissues, we evaluated the relative prognostic significance of neutrophil infiltration and *Fusobacterium nucleatum* loads in a well-characterized tissue microarray (TMA) including >500 CRC cases[13,14,16] (Table S7) and in the publicly available TCGA database. High densities of CRC-TANs, as detected by high numbers of CD66b+ cells in the TMA, were significantly associated with improved overall survival in both univariate and multivariate analyses (Figures 7A and S7A). Consistently, high expression of *CEACAM8* in TCGA was also predictive of improved clinical outcome (Figure 7B). In contrast, tumor colonization by high *Fusobacterium nucleatum* loads, as assessed by fluorescence *in situ* hybridization (FISH) in the TMA, did not show any significant association with survival per se. Instead, in TCGA, high CRC colonization by *Fusobacterium nucleatum*, as assessed based on RNA transcripts in The Cancer Microbiome Atlas (TCMA),[42] showed a trend toward association with improved clinical outcome (Figures 7C, 7D, and S7B). Remarkably, in the TMA cohort, the positive prognostic significance of neutrophil infiltration appeared to be dependent on *Fusobacterium nucleatum* presence, as it was dramatically reduced in CRC cases with absent/low *Fusobacterium nucleatum* loads (Figures 7E, S7C, and S7D). A similar trend was observed in TCGA, although no statistical significance was achieved (Figure 7F).

Finally, we assessed the clinical relevance of *SIGLEC14* expression. In TCGA database, we identified a subgroup of patients (n = 31) whose tumors selectively lack expression of *SIGLEC14* (Figure 7G), despite retaining *CEACAM8* and *SIGLEC5* expression (Figures S7F and S7G). Notably, this subgroup exhibited significantly reduced overall survival compared with patients with preserved *SIGLEC14* expression (Figure 7H), thus strongly supporting the functional and prognostic importance of Siglec-14 in CRC.

DISCUSSION

A high density of TANs in the TME is widely considered to be associated with immunosuppression and to promote tumor progression.[48] However, a number of recent studies have documented TANs' antitumor potential,[19–23,25,49] and in human CRC, TAN infiltration has been reported to be associated with either favorable or unfavorable clinical outcomes.[10–12,15–17] Nevertheless, stimuli potentially eliciting cytotoxic functions in neutrophils and factors determining their prognostic significance remain unclear.

In this study we unraveled how neutrophil functional profiles are steered by bacterial components of the intratumoral microbiota and that only defined bacterial taxa are able to unleash neutrophil cytotoxic potential. Paradoxically, we found that among the most abundant bacteria of the intratumoral CRC microbiota, *Fusobacterium nucleatum*, a known pathogenic bacterium, but not *Bacteroides fragilis*, efficiently recruits neutrophils into tumor beds and triggers them to release cytotoxic factors mediating tumor cell killing *in vitro* and *in vivo*. Accordingly, high CRC colonization by *Fusobacterium nucleatum* improves the positive prognostic significance of TANs, as assessed in a TMA, including 444 CRC patients. Most importantly, mechanistically, we demonstrated that *Fusobacterium nucleatum*-neutrophil interaction is mediated by Siglec-14, as *Fusobacterium nucleatum*-induced neutrophil activation is abrogated in the presence of Siglec-14-neutralizing antibodies or in responders carrying a loss-of-function Siglec-14 polymorphism. scRNA-seq and protein analyses confirmed activation of Siglec-14 downstream pathways specifically following *Fusobacterium nucleatum* activation and in Siglec-14 WT donors only. Importantly, transcription signatures associated with Siglec-14 pathway activation were also detected in TANs from primary CRC tissues. Consistently, lack of *SIGLEC14* expression is associated with reduced survival probability in patients with CRC.

(B) Percentages of tumor cell killing detected upon incubation of LS180 with supernatants from bacteria-stimulated PBNs from all HDs and patients assessed, as stratified according to donors' Siglec-14 genotype (WT/WT, n = 10; heterozygous, WT/null, n = 9; null/null, n = 5). Statistical significance was assessed by Tukey's multiple comparison test (****$p < 0.0001$).

(C) Western blot analysis showing phosphorylation of p38 and ERK in untreated, *Bacteroides fragilis*- or *Fusobacterium nucleatum*-stimulated neutrophils from Siglec-14 WT or null donors.

(D–G) Single-cell RNA-seq analysis of untreated, *Bacteroides fragilis* or *Fusobacterium nucleatum*-stimulated neutrophils from a Siglec-14 WT or null donor. (D) Uniform manifold approximation and projection (UMAP) showing identified clusters. (E) Differential gene expression analysis in untreated, *Bacteroides fragilis*- or *Fusobacterium nucleatum*-stimulated neutrophils. Data refer to average expression levels and percentages of positive cells within each group. (F) UMAP showing identified clusters based on treatment and Siglec-14 genotype. (G) GO analysis on cluster 3 showing pathways differentially activated in Siglec-14 WT and null neutrophils. Fn, *Fusobacterium nucleatum*; Bf, *Bacteroides fragilis*.

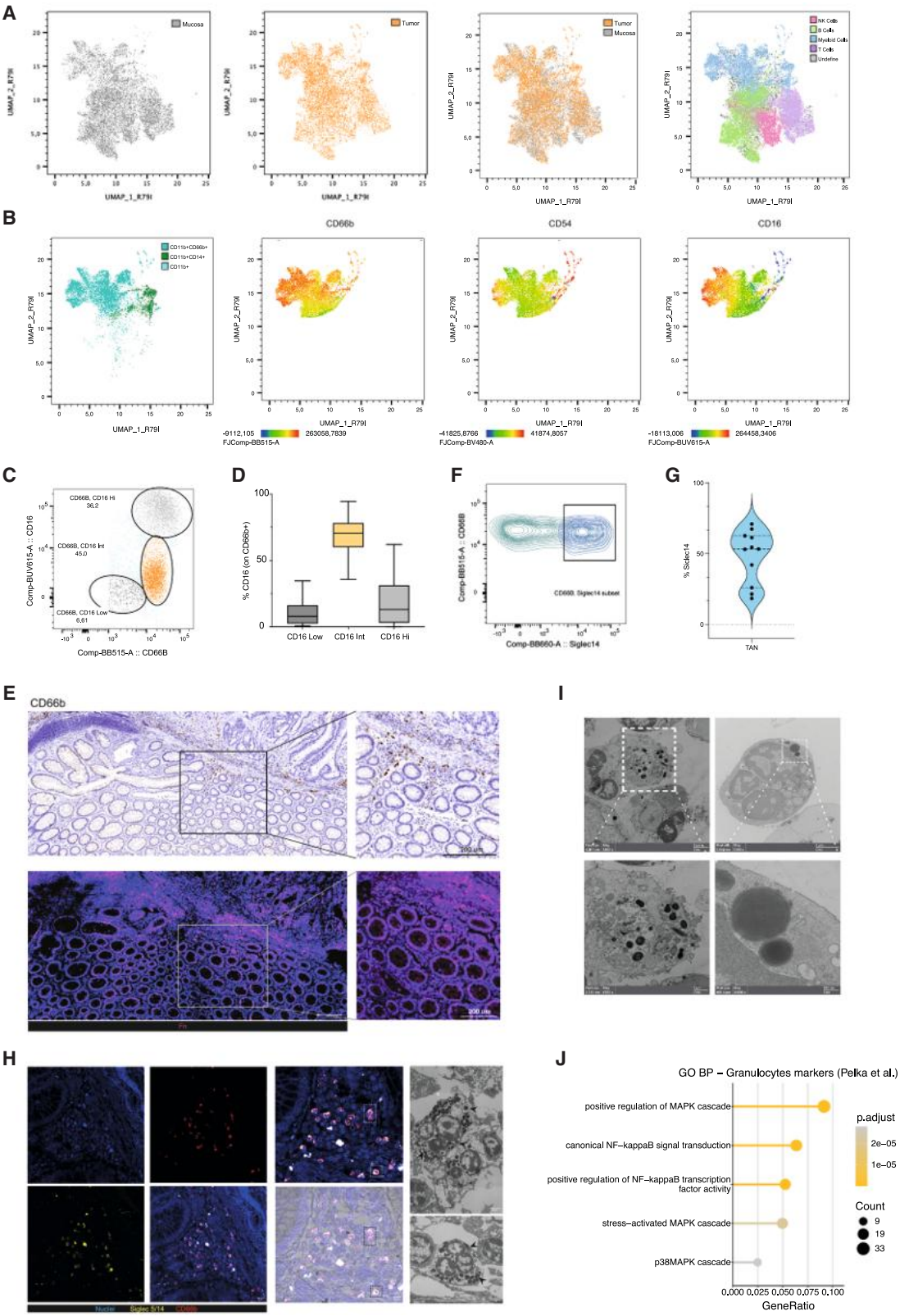

Figure 6. Phenotypic and transcriptional analysis of TANs from human primary CRCs

(A–D) Single-cell suspensions were obtained from freshly resected specimens of primary CRC and corresponding healthy colonic tissues following enzymatic digestion (cohort 3, $n = 34$). Large-scale flow cytometry was performed upon staining with specific antibodies (see key resources table). (A) UMAP cluster analysis

(legend continued on next page)

Altogether, our findings identify microbiota composition and host genetic profile as key factors influencing TANs' functional potential.

The ability of *Fusobacterium nucleatum* and other bacteria to stimulate chemokine production in tumor cells has previously been documented,[36–38] but their relative effectiveness has not been comparatively evaluated. Unexpectedly, we found that, in comparison with *Bacteroides fragilis*, *Fusobacterium nucleatum* most efficiently promotes neutrophil recruitment by stimulating chemokine production by tumor cells. Moreover, *Fusobacterium nucleatum* effectively triggers the elicitation of neutrophils' cytotoxic functions.

Fusobacterium nucleatum powerfully modulated phenotypic profiles of PBNs from patients and HDs by inducing upregulation of CD66b and CD54, and downregulation of CD16 and CD62L, resulting in the expression of a CD66b high/CD16 intermediate phenotype, whereas *Bacteroides fragilis* only elicited minor effects.

Notably, *Fusobacterium nucleatum* has consistently been reported to mediate pro-tumorigenic effects *in vitro* and in mouse models,[28–30] and this activity has been proposed to be due to its capacity to invade tumor cells.[26–28,30] However, gut colonization by *Fusobacterium nucleatum* has recently been suggested to be associated with responsiveness to ICIs in human microsatellite-stable (MSS) CRC.[50] In contrast, the outcome of *Fusobacterium nucleatum* interaction with CRC-derived TANs has not been thoroughly investigated so far.

Here, we provide evidence that *Fusobacterium nucleatum* induces in neutrophils a so-called "vital NETosis," characterized by the release of extracellular traps, composed of nuclear DNA, through nuclear membrane vesiculation and vesicular export, in the absence of plasma membrane rupture.[43] More importantly, we observed that *Fusobacterium nucleatum*, but not *Bacteroides fragilis*, triggers in neutrophils the release of a cocktail of cytotoxic factors, including MMP8 and 9, lipocalin-2, elastase, defensin A1, cathelicidin, and myeloperoxidase (MPO), promoting tumor cell death.

Previous studies have highlighted the antitumor potential of some of these factors. Human neutrophil-derived elastase was shown to induce death of different types of tumor cells and to inhibit primary tumor growth in a mouse model.[19] Notably, elastase is not produced by murine neutrophils.[19] Moreover, cathelicidin was also reported to induce apoptosis in human CRC cells.[51] On the other hand, CRC cells overexpressing lipocalin-2 were previously shown to be characterized by limited proliferation and metastatic potential compared with control cells.[52,53] However, the stimuli triggering the release of these molecules within the CRC microenvironment had not thus far been clarified.

Our findings delineate a scenario in which these factors are released within the CRC TME upon interaction between TANs and selected bacterial species, such as *Fusobacterium nucleatum* or, possibly, other bacteria. Thus, gut microbiota composition may critically impact not only TAN recruitment but also the elicitation of their cytotoxic functions.

The ability of neutrophils to mediate tumor cell killing upon *Fusobacterium nucleatum* stimulation might explain the reported association of TANs with a more favorable clinical outcome in CRC. Indeed, the analysis of our own TMA cohort and of publicly available databases indicates that, in the absence of high *Fusobacterium nucleatum* loads, TANs' positive prognostic significance is significantly reduced.

Admittedly, studies investigating TANs' prognostic significance in human CRC have so far provided contradictory results.[48] The heterogeneity of the methodologies used for investigation, e.g., IHC staining of neutrophil-specific[10–12,15–17] versus-related markers,[14,54] or evaluation of expression levels of different panels of neutrophil-related genes,[55,56] may partially account for these discrepancies. However, different results have also emerged in studies assessing neutrophil infiltration with similar technologies. For instance, in three studies from European countries, i.e., Italy, including 178 patients,[15] Switzerland (n = 650),[16] and Sweden (n = 448),[17] TME densities of CD66b+ cells, assessed by IHC staining, were found to be associated with improved overall[16] and disease-free survival, irrespective of disease stage.[15,17] In line with these results, in the COAD-READ cohorts of TCGA database, including patients from the US, the expression of genes encoding neutrophil-recruiting chemokines, such as *CXCL1*, *CXCL2*, *CXCL5*, and *CXCL8*, is also associated with favorable prognosis. In contrast, in studies evaluating patient cohorts from Guangzhou,[10] Bengbu,[11] and Shanghai,[12] all in the People's Republic of China, CRC infiltration by CD66b+ cells has been reported to correlate with reduced disease-free survival. In this context, our study, identifying Siglec-14 as a key mediator of bacteria-induced neutrophil cytotoxic effects, might offer an innovative interpretation that potentially reconciles these discrepancies.

of $CD45^+$ live cells within concatenated healthy colonic tissues and corresponding primary CRC (n = 34). The indicated immune cell subsets are identified by specific colors. (B) Among $CD11b^+$ myeloid cells, neutrophils and monocytes are identified based on $CD11b^+$ $CD66b^+$ and $CD11b^+$ $CD14^+$ phenotypes, respectively. Expression of CD66b, CD54, and CD16 markers within the neutrophil cell cluster is depicted. (C and D) Representative dot plot (C) and percentages (D) of neutrophil subsets identified among TANs based on CD16 expression levels.

(E) Upper: CRC-infiltrating TANs were identified by IHC staining of CD66b. Lower: *Fusobacterium nucleatum* was visualized by RNAscope. Representative pictures at 10× magnification showing TAN and *Fusobacterium nucleatum* infiltration within the same tissue area are depicted.

(F) Representative dot plots of Siglec-14 staining on CRC-infiltrating TANs.

(G) Percentages of Siglec-14^+ TANs detected in CRC cell suspensions (n = 11) by flow cytometry.

(H) Left: immunofluorescence staining of Siglec-5/14 (yellow), CD66b (red), and DAPI (blue) was performed on FFPE-CRC tissues. Representative pictures of Siglec-5/14 expression on TANs at 40× magnification are shown. Right: the same tissue slides were evaluated by CLEM. Pictures show ultracellular structure of identified TANs. Arrows indicate internalized bacteria.

(I) TANs were sorted from CRC cell suspensions, based on $CD11b^+$ $CD66b^+$ phenotype, and evaluated by TEM analysis. Representative images showing putative vital NETosis and bacterial internalization (indicated by arrows) are depicted. Upper: magnification 3,400–5,300×; lower: magnification 6,700–36,000×.

(J) GO analysis of a previously published scRNA-seq database from human CRC tissues[40] showing mostly upregulated signaling pathways in cells classified as "granulocytes."

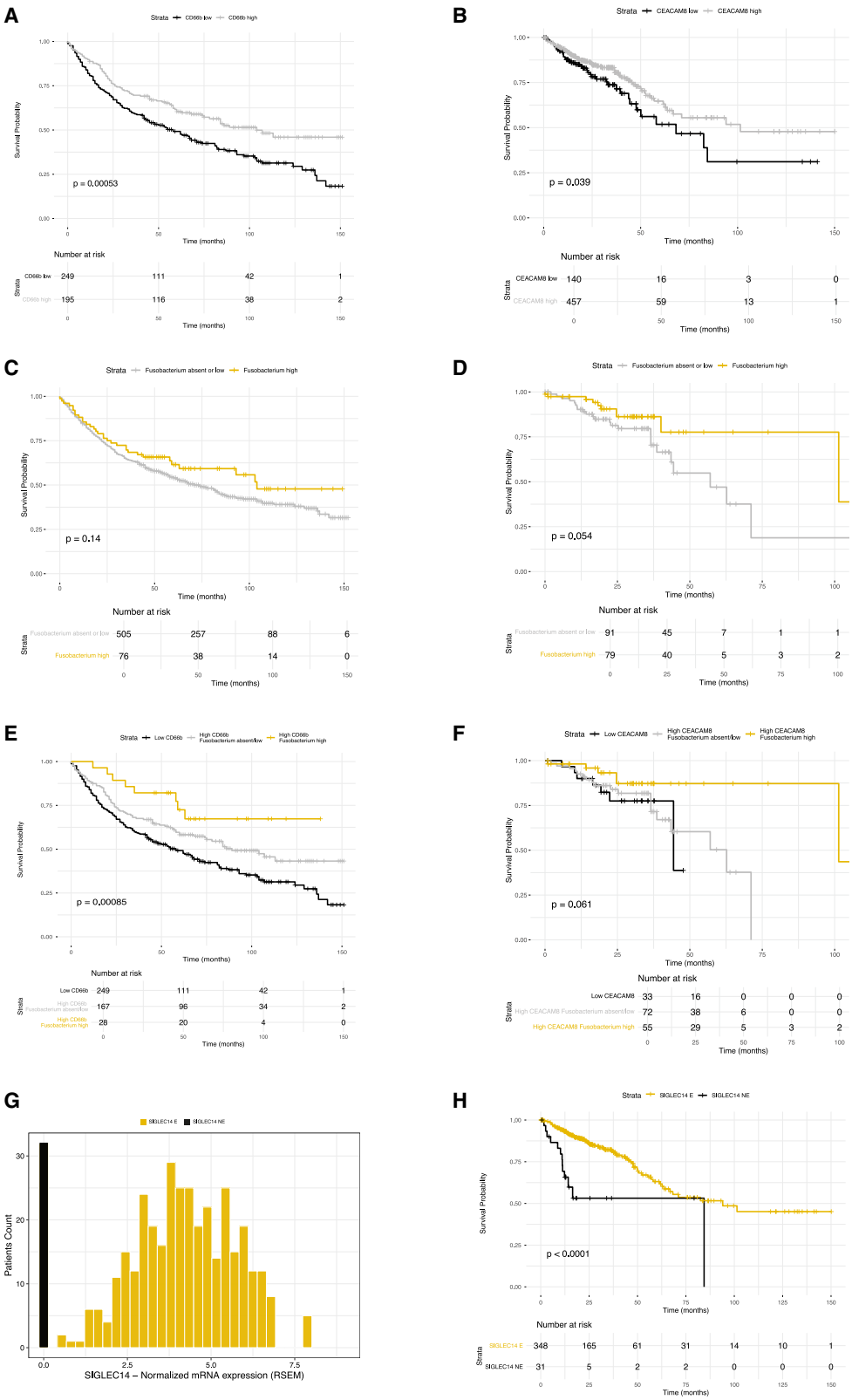

Figure 7. Prognostic significance of CRC infiltration by TANs and *Fusobacterium nucleatum*

The prognostic significance of CRC infiltration by TANs and *Fusobacterium nucleatum* was evaluated in a tissue microarray (TMA, A, C, and E) including 444 primary CRC cases (Table S7) and in the COAD-READ cohort of TCGA databases (B, D, and F–H). Fn, *Fusobacterium nucleatum*.

(legend continued on next page)

Siglec-14 represents an important exception within the Siglec family, as, in contrast to the other family members, it is devoid of an intracellular ITIM domain and is rather associated with DAP12, displaying an activating ITAM.[46]

Siglec-14 did not appear to be responsible for neutrophil phenotypic modulation occurring upon *Fusobacterium nucleatum* stimulation, which, instead, was clearly dependent on TLR4 engagement. However, Siglec-14 appeared to play a critical role in the elicitation of neutrophils' cytotoxic effects, which were fully abrogated in the presence of specific neutralizing antibodies or were missing in neutrophils from donors carrying a common genetic polymorphism leading to loss of function of Siglec-14.[47]

Most interestingly, this polymorphism has been reported to occur in <10% of Europeans but in up to 70% of East Asian populations.[47] It is therefore reasonable to hypothesize that, in most European patients with CRC, the interaction between *Fusobacterium nucleatum* and TANs expressing Siglec-14^{WT} might result in the release of cytotoxic factors, potentially promoting antitumor effects. Conversely, in most Asian patients, the exposure of Siglec-14^{Null} -carrying TANs to *Fusobacterium nucleatum* might fail to induce cytotoxic activity, thereby allowing *Fusobacterium nucleatum*-mediated pro-tumorigenic effects to predominate and ultimately to negatively impact patients' survival. Whether *Fusobacterium nucleatum*-initiated signaling through Siglec-5 in the absence of Siglec-14 might additionally elicit immune-suppressive functions in TANs from these patients remains to be explored.

Collectively, our findings suggest that several factors concur to influence CRC clinical outcome. Besides TME and intratumoral microbiota composition, polymorphisms of genes involved in the innate immune response may critically influence prognosis. Notably, TLR4, which we found to mediate neutrophil phenotypic modulation in response to *Fusobacterium nucleatum*, and other TLRs also harbor different polymorphic variants, which have been suggested to be differentially associated with CRC development and progression.[57,58] Finally, tumor cell genomic and epigenomic instability, leading to amplification, deletion, or silencing of chemokine genes,[59–61] might also shape the CRC immune context and, ultimately, the clinical outcome.

Our data also urge caution in the interpretation of results regarding CRC-neutrophil interactions emerging from experimental animal models.[62] Neutrophils from humans and experimental animals are known to present major differences.[63] For instance, elastase and defensins are released by human neutrophils upon *Fusobacterium nucleatum* activation but are not produced by murine neutrophils. Also, chemokines and chemokine receptors playing key roles in the interaction between CRC cells and neutrophils, such as CXCL8 and its receptor CXCR1, are not expressed by murine neutrophils.[19,64] Most importantly, Siglecs' expression largely differs between human and murine neutrophils. Indeed, the latter do not express Siglec-14 or any other activating Siglec. Instead, they are known to express Siglec-E, the ortholog of human Siglec-9, and, in the TME, Siglec-F,[65] both containing ITIM motifs and thereby transmitting inhibitory signals.[46] Accordingly, in our study, murine neutrophils failed to display cytotoxic activity upon *Fusobacterium nucleatum* exposure.

On the other hand, the impossibility of validating our findings in a microbiota-controlled syngeneic mouse CRC model represents the most important limitation of our study. Although humanized mouse models may represent an interesting alternative experimental approach, currently available models achieve limited reconstitution of PBNs, not exceeding 30% of white blood cells, as compared with 50%–70% detectable in healthy humans.[66,67] Therefore, to fully recapitulate functional neutrophil-driven antitumor responses in experimental animals, the implementation of multiple novel strategies is needed.[67]

Further research is also warranted to identify bacterial molecular determinants responsible for Siglec-14 triggering. Although we observed Siglec-14 binding to *Fusobacterium nucleatum*-derived LPS, the specific glycan structures involved remain to be fully characterized.

In addition, although *Fusobacterium nucleatum* and *Bacteroides fragilis*, as major components of CRC-associated microbiota, represent the focus of our study, additional species other than *Fusobacterium nucleatum* might be able to trigger Siglec-14-mediated neutrophil activation[68,69] and possibly synergize with *Fusobacterium nucleatum* in modulating neutrophil functions. Indeed, microbial consortia have been described within CRC-associated intratumoral microbiota, and their composition may also vary according to tumor localization within the intestinal tract.[70,71] The investigation of their potential antitumor functions could be of high interest, as bacterial species inducing tumor cytotoxicity, without being associated with the potentially protumoral effects of *Fusobacterium nucleatum*, might qualify for clinical studies. On the other hand, the impact of antibiotic treatment on *Fusobacterium nucleatum*-mediated neutrophil activation in CRC patients also deserves to be explored.[72]

Nevertheless, our findings provide important suggestions for innovative immunotherapy treatments beyond adaptive immunity. In patients expressing WT Siglec-14, adequate conditioning of gut microbiota might result in the successful elicitation of neutrophil-mediated antitumor effects.

Therapies taking advantage of neutrophil activation could also complement currently available immunotherapies based on ICIs, considering that synergisms between granulocytes and T cells in the elicitation of antitumor effects have previously

(A and B) Kaplan-Meier curves illustrating overall survival (OS) probability in patients stratified according to TAN density (high versus low), as assessed by numbers of CD66b$^+$ cells in the TMA (A) and by *CEACAM8* gene expression levels in TCGA (B, n = 597).

(C and D) Kaplan-Meier survival curves showing OS in patients stratified according to *Fusobacterium nucleatum* abundance (absent/low versus high) as evaluated by FISH in the TMA (C) and annotated in The Cancer Microbiome Atlas (TCMA, n = 170, D).

(E and F) Kaplan-Meier survival curves showing OS in patients stratified based on TAN density and *Fusobacterium nucleatum* abundance (CD66b or *CEACAM8*^{high}/Fn^{high}, CD66b or *CEACAM8*^{high}/Fn$^{absent/low}$, CD66b or *CEACAM8*^{low}) in the TMA (E) or in TCGA (F).

(G) Histogram showing the distribution of normalized mRNA expression (RSEM, $\log_2$) of *SIGLEC14* across patients in the COAD-READ cohort of TCGA.

(H) Kaplan-Meier OS curves comparing patients with *SIGLEC14* expression =0 (SIGLEC14-NE) and >0 (SIGLEC14-E) in the COAD-READ TCGA cohort (TCGA, Firehose Legacy). Survival differences were assessed using the log-rank test. Tables show numbers of patients alive and at risk of death at each time point after CRC diagnosis.

been reported.[16,73–75] Notably, *Fusobacterium nucleatum* has recently been shown to enhance responsiveness to ICIs in a MSS CRC mouse model.[50]

In conclusion, our work identifies both intratumoral microbiota composition and the host genetic makeup as critical factors for the elicitation of neutrophil cytotoxic effects and unravels Siglec-14 as a potential therapeutic target for the development of innovative immunotherapies unleashing TANs' cytotoxic potential.

RESOURCE AVAILABILITY

Lead contact

Further information and requests for resources and reagents should be directed to and will be fulfilled by the lead contact, Giandomenica Iezzi (giandomenica.iezzi@usi.ch).

Materials availability

All unique materials generated in this study are available from the lead contact upon reasonable request and completion of a materials transfer agreement.

Data and code availability

All software packages used are publicly available through nonprofit databases and commercial vendors.

- The mass spectrometry proteomics data have been deposited in the ProteomeXchange Consortium via the PRIDE partner repository with the dataset identifier PRIDE: PXD069316 (token: TaIFl6oL7Jo5).
- The single-cell data from Rhapsody have been deposited in GEO with the dataset identifier GEO: GSE311000.
- All other items: additional resources are referenced in the key resources table.
- Any additional information required to reanalyze the data reported in this paper is available from the lead contact upon request.

ACKNOWLEDGMENTS

We thank the patients and their families. We are grateful to Prof. Raoul Droeser and Prof. Daniel Oertli (University Hospital Basel, Basel, Switzerland) for contributing to the collection of tissue samples and to Simone Keck and Virginie Galati (University Children's Hospital Basel, Switzerland) for help with FISH validation. We are also thankful to all members of Bios+ facilities, in particular to David Jarossay for help with flow cytometry cell sorting, Matteo Pecoraro for assistance with proteomics analysis, Andrea Raimondi for TEM imaging, Simone Mosole for help with IHC and RNAscope, Diego Morone for technical support with confocal imaging, and Gianluca Civenni for helping with *in vivo* imaging. This project was supported by the Swiss National Science Foundation (grant no. 310030_185234 to G.I.), the Novartis Foundation for Medical-Biological Research (grant no. 25B048 to G.I.), the Associazione Italiana per la Ricerca sul Cancro (AIRC, grant no. 2020-24440 to G.S.), and the German Research Foundation (DFG, project no. 395357507-SFB 1371 to K.-P.J.).

AUTHOR CONTRIBUTIONS

Conceptualization, E.S., V.G., G.S., P.E.M.-H., L.B., G.C.S., D. Christoforidis, and G.I.; methodology, E.S., V.G., D.B., E.C., N.F., I.L., B.C., C.T., C.B., C.S., F. Cetti, D. Calabrese, C.E., F.M., L.T., V.M., E.P., M.T., L.B., K.-P.J., M.F., F. Chiacchiera, J.-P.T., S.F.G., S.E.-C., and L.M.T.; investigation, E.S., V.G., D.B., E.C., N.F., I.L., B.C., C.T., C.B., J.G., M.V., C.S., F. Cetti, D. Calabrese, C.E., V.M., E.P., J.D., A.C., L.B., K.-P.J., M.F., F. Chiacchiera, L.T., S.F.G., S.D.D., S.E.-C., L.M.T., G.C.S., and G.I.; visualization, E.S., V.G., D.B., E.C., I.L., B.C., C.T., C.E., F. Chiacchiera, S.F.G., S.E.-C., and G.I.; funding acquisition, E.S., P.E.M.-H., D.C., and G.I.; project administration, P.E.M.-H., D. Christoforidis, and G.I.; supervision, G.I.; writing – original draft, E.S. and G.I.; writing – review & editing, E.S., V.G., D.B., E.C., I.L., B.C., C.T., J.G., M.V., D.C., C.E., F.M., C.B., V.M., J.D., A.C., M.T., G.S., L.B., K.-P.J., M.F., F. Chiacchiera, S.F.G., S.D.D., S.E.-C., L.M.T., P.E.M.-H., G.C.S., D. Chrisoforidis, and G.I.

DECLARATION OF INTERESTS

The authors declare no competing interests.

STAR★METHODS

Detailed methods are provided in the online version of this paper and include the following:

- KEY RESOURCES TABLE
- EXPERIMENTAL MODEL AND STUDY PARTICIPANT DETAILS
  - Clinical specimen collection and processing
  - Cell lines
  - Animals
  - Bacteria
  - Neutrophils and bacteria co-cultures
- METHOD DETAILS
  - RNA isolation and Real-time reverse transcription PCR assays
  - scRNA-seq dataset analysis
  - Tumor cells and bacteria coculture
  - Migration Assay
  - Flow cytometry
  - Western Blot Analysis
  - Proteomic analysis
  - Transmission Electron Microscopy
  - Correlative Light Electron Microscopy (CLEM) on FFPE tissue sections
  - Cytotoxic activity of culture supernatants
  - Siglec-5/14 Genotyping
  - LPS purification
  - ELISA analysis of bacterial LPS
  - PEI-mediated transfection and lentiviral infection
  - Plasmids
  - Immunofluorescence microscopy
  - Live imaging
  - RNAscope
  - Immunohistochemistry
  - Rhapsody
  - BD Rhapsody™ Whole Transcriptome Analysis (WTA)
  - TMA construction
  - Fn detection in CRC TMA by FISH
  - Survival analyses in TMA
  - Survival Analysis in TCGA
- QUANTIFICATION STATISTICAL ANALYSIS

SUPPLEMENTAL INFORMATION

Supplemental information can be found online at https://doi.org/10.1016/j.chom.2026.02.006.

Received: May 5, 2025
Revised: December 23, 2025
Accepted: February 4, 2026
Published: March 11, 2026

REFERENCES

1. Swanton, C., Bernard, E., Abbosh, C., André, F., Auwerx, J., Balmain, A., Bar-Sagi, D., Bernards, R., Bullman, S., DeGregori, J., et al. (2024). Embracing cancer complexity: Hallmarks of systemic disease. Cell *187*, 1589–1616. https://doi.org/10.1016/j.cell.2024.02.009.
2. Fridman, W.H., Pagès, F., Sautès-Fridman, C., and Galon, J. (2012). The immune contexture in human tumours: impact on clinical outcome. Nat. Rev. Cancer *12*, 298–306. https://doi.org/10.1038/nrc3245.

3. Bruni, D., Angell, H.K., and Galon, J. (2020). The immune contexture and Immunoscore in cancer prognosis and therapeutic efficacy. Nat. Rev. Cancer *20*, 662–680. https://doi.org/10.1038/s41568-020-0285-7.

4. Grivennikov, S.I., Wang, K., Mucida, D., Stewart, C.A., Schnabl, B., Jauch, D., Taniguchi, K., Yu, G.-Y., Österreicher, C.H., Hung, K.E., et al. (2012). Adenoma-linked barrier defects and microbial products drive IL-23/IL-17-mediated tumour growth. Nature *491*, 254–258. https://doi.org/10.1038/nature11465.

5. Jackstadt, R., van Hooff, S.R., Leach, J.D., Cortes-Lavaud, X., Lohuis, J.O., Ridgway, R.A., Wouters, V.M., Roper, J., Kendall, T.J., Roxburgh, C.S., et al. (2019). Epithelial NOTCH Signaling Rewires the Tumor Microenvironment of Colorectal Cancer to Drive Poor-Prognosis Subtypes and Metastasis. Cancer Cell *36*, 319–336.e7. https://doi.org/10.1016/j.ccell.2019.08.003.

6. Metzger, R., Maruskova, M., Krebs, S., Janssen, K.-P., and Krug, A.B. (2019). Increased Incidence of Colon Tumors in AOM-Treated Apc1638N/+ Mice Reveals Higher Frequency of Tumor Associated Neutrophils in Colon Than Small Intestine. Front. Oncol. *9*, 1001. https://doi.org/10.3389/fonc.2019.01001.

7. Itatani, Y., Yamamoto, T., Zhong, C., Molinolo, A.A., Ruppel, J., Hegde, P., Taketo, M.M., and Ferrara, N. (2020). Suppressing neutrophil-dependent angiogenesis abrogates resistance to anti-VEGF antibody in a genetic model of colorectal cancer. Proc. Natl. Acad. Sci. USA *117*, 21598–21608. https://doi.org/10.1073/pnas.2008112117.

8. Liao, W., Overman, M.J., Boutin, A.T., Shang, X., Zhao, D., Dey, P., Li, J., Wang, G., Lan, Z., Li, J., et al. (2019). KRAS-IRF2 Axis Drives Immune Suppression and Immune Therapy Resistance in Colorectal Cancer. Cancer Cell *35*, 559–572.e7. https://doi.org/10.1016/j.ccell.2019.02.008.

9. Germann, M., Zangger, N., Sauvain, M.O., Sempoux, C., Bowler, A.D., Wirapati, P., Kandalaft, L.E., Delorenzi, M., Tejpar, S., Coukos, G., et al. (2020). Neutrophils suppress tumor-infiltrating T cells in colon cancer via matrix metalloproteinase-mediated activation of TGFβ. EMBO Mol. Med. *12*, e10681. https://doi.org/10.15252/emmm.201910681.

10. Rao, H.-L., Chen, J.-W., Li, M., Xiao, Y.-B., Fu, J., Zeng, Y.-X., Cai, M.-Y., and Xie, D. (2012). Increased Intratumoral Neutrophil in Colorectal Carcinomas Correlates Closely with Malignant Phenotype and Predicts Patients' Adverse Prognosis. PLoS One *7*, e30806. https://doi.org/10.1371/journal.pone.0030806.

11. Zhu, B., Luo, J., Jiang, Y., Yu, L., Liu, M., and Fu, J. (2018). Prognostic significance of nomograms integrating IL-37 expression, neutrophil level, and MMR status in patients with colorectal cancer. Cancer Med. *7*, 3682–3694. https://doi.org/10.1002/cam4.1663.

12. Hu, X., Li, Y.-Q., Ma, X.-J., Zhang, L., Cai, S.-J., and Peng, J.-J. (2019). A Risk Signature With Inflammatory and T Immune Cells Infiltration in Colorectal Cancer Predicting Distant Metastases and Efficiency of Chemotherapy. Front. Oncol. *9*, 704. https://doi.org/10.3389/fonc.2019.00704.

13. Sconocchia, G., Zlobec, I., Lugli, A., Calabrese, D., Iezzi, G., Karamitopoulou, E., Patsouris, E.S., Peros, G., Horcic, M., Tornillo, L., et al. (2011). Tumor infiltration by FcγRIII (CD16)+ myeloid cells is associated with improved survival in patients with colorectal carcinoma. Int. J. Cancer *128*, 2663–2672. https://doi.org/10.1002/ijc.25609.

14. Droeser, R.A., Hirt, C., Eppenberger-Castori, S., Zlobec, I., Viehl, C.T., Frey, D.M., Nebiker, C.A., Rosso, R., Zuber, M., Amicarella, F., et al. (2013). High Myeloperoxidase Positive Cell Infiltration in Colorectal Cancer Is an Independent Favorable Prognostic Factor. PLoS One *8*, e64814. https://doi.org/10.1371/journal.pone.0064814.

15. Galdiero, M.R., Bianchi, P., Grizzi, F., Di Caro, G., Basso, G., Ponzetta, A., Bonavita, E., Barbagallo, M., Tartari, S., Polentarutti, N., et al. (2016). Occurrence and significance of tumor-associated neutrophils in patients with colorectal cancer. Int. J. Cancer *139*, 446–456. https://doi.org/10.1002/ijc.30076.

16. Governa, V., Trella, E., Mele, V., Tornillo, L., Amicarella, F., Cremonesi, E., Muraro, M.G., Xu, H., Droeser, R., Däster, S.R., et al. (2017). The Interplay Between Neutrophils and CD8+ T Cells Improves Survival in Human Colorectal Cancer. Clin. Cancer Res. *23*, 3847–3858. https://doi.org/10.1158/1078-0432.CCR-16-2047.

17. Wikberg, M.L., Ling, A., Li, X., Öberg, Å., Edin, S., and Palmqvist, R. (2017). Neutrophil infiltration is a favorable prognostic factor in early stages of colon cancer. Hum. Pathol. *68*, 193–202. https://doi.org/10.1016/j.humpath.2017.08.028.

18. Berry, R.S., Xiong, M.-J., Greenbaum, A., Mortaji, P., Nofchissey, R.A., Schultz, F., Martinez, C., Luo, L., Morris, K.T., and Hanson, J.A. (2017). High levels of tumor-associated neutrophils are associated with improved overall survival in patients with stage II colorectal cancer. PLoS One *12*, e0188799. https://doi.org/10.1371/journal.pone.0188799.

19. Cui, C., Chakraborty, K., Tang, X.A., Zhou, G., Schoenfelt, K.Q., Becker, K.M., Hoffman, A., Chang, Y.-F., Blank, A., Reardon, C.A., et al. (2021). Neutrophil elastase selectively kills cancer cells and attenuates tumorigenesis. Cell *184*, 3163–3177.e21. https://doi.org/10.1016/j.cell.2021.04.016.

20. Ponzetta, A., Carriero, R., Carnevale, S., Barbagallo, M., Molgora, M., Perucchini, C., Magrini, E., Gianni, F., Kunderfranco, P., Polentarutti, N., et al. (2019). Neutrophils Driving Unconventional T Cells Mediate Resistance against Murine Sarcomas and Selected Human Tumors. Cell *178*, 346–360.e24. https://doi.org/10.1016/j.cell.2019.05.047.

21. Wu, Y., Ma, J., Yang, X., Nan, F., Zhang, T., Ji, S., Rao, D., Feng, H., Gao, K., Gu, X., et al. (2024). Neutrophil profiling illuminates anti-tumor antigen-presenting potency. Cell *187*, 1422–1439.e24. https://doi.org/10.1016/j.cell.2024.02.005.

22. Gungabeesoon, J., Gort-Freitas, N.A., Kiss, M., Bolli, E., Messemaker, M., Siwicki, M., Hicham, M., Bill, R., Koch, P., Cianciaruso, C., et al. (2023). A neutrophil response linked to tumor control in immunotherapy. Cell *186*, 1448–1464.e20. https://doi.org/10.1016/j.cell.2023.02.032.

23. Hirschhorn, D., Budhu, S., Kraehenbuehl, L., Gigoux, M., Schröder, D., Chow, A., Ricca, J.M., Gasmi, B., De Henau, O., Mangarin, L.M.B., et al. (2023). T cell immunotherapies engage neutrophils to eliminate tumor antigen escape variants. Cell *186*, 1432–1447.e17. https://doi.org/10.1016/j.cell.2023.03.007.

24. Linde, I.L., Prestwood, T.R., Qiu, J., Pilarowski, G., Linde, M.H., Zhang, X., Shen, L., Reticker-Flynn, N.E., Chiu, D.K.-C., Sheu, L.Y., et al. (2023). Neutrophil-activating therapy for the treatment of cancer. Cancer Cell *41*, 356–372.e10. https://doi.org/10.1016/j.ccell.2023.01.002.

25. Ng, M., Cerezo-Wallis, D., Ng, L.G., and Hidalgo, A. (2025). Adaptations of neutrophils in cancer. Immunity *58*, 40–58. https://doi.org/10.1016/j.immuni.2024.12.009.

26. El Tekle, G., Andreeva, N., and Garrett, W.S. (2024). The Role of the Microbiome in the Etiopathogenesis of Colon Cancer. Annu. Rev. Physiol. *86*, 453–478. https://doi.org/10.1146/annurev-physiol-042022-025619.

27. White, M.T., and Sears, C.L. (2024). The microbial landscape of colorectal cancer. Nat. Rev. Microbiol. *22*, 240–254. https://doi.org/10.1038/s41579-023-00973-4.

28. Rubinstein, M.R., Wang, X., Liu, W., Hao, Y., Cai, G., and Han, Y.W. (2013). Fusobacterium nucleatum Promotes Colorectal Carcinogenesis by Modulating E-Cadherin/β-Catenin Signaling via its FadA Adhesin. Cell Host Microbe *14*, 195–206. https://doi.org/10.1016/j.chom.2013.07.012.

29. Kostic, A.D., Chun, E., Robertson, L., Glickman, J.N., Gallini, C.A., Michaud, M., Clancy, T.E., Chung, D.C., Lochhead, P., Hold, G.L., et al. (2013). Fusobacterium nucleatum Potentiates Intestinal Tumorigenesis and Modulates the Tumor-Immune Microenvironment. Cell Host Microbe *14*, 207–215. https://doi.org/10.1016/j.chom.2013.07.007.

30. Gur, C., Ibrahim, Y., Isaacson, B., Yamin, R., Abed, J., Gamliel, M., Enk, J., Bar-On, Y., Stanietsky-Kaynan, N., Coppenhagen-Glazer, S., et al. (2015). Binding of the Fap2 Protein of Fusobacterium nucleatum to Human Inhibitory Receptor TIGIT Protects Tumors from Immune Cell Attack. Immunity *42*, 344–355. https://doi.org/10.1016/j.immuni.2015.01.010.

31. Dadgar-Zankbar, L., Elahi, Z., Shariati, A., Khaledi, A., Razavi, S., and Khoshbayan, A. (2024). Exploring the role of Fusobacterium nucleatum in colorectal cancer: implications for tumor proliferation and

chemoresistance. Cell Commun. Signal. *22*, 547. https://doi.org/10.1186/s12964-024-01909-y.

32. Ou, S., Wang, H., Tao, Y., Luo, K., Ye, J., Ran, S., Guan, Z., Wang, Y., Hu, H., and Huang, R. (2022). Fusobacterium nucleatum and colorectal cancer: From phenomenon to mechanism. Front. Cell. Infect. Microbiol. *12*, 1020583. https://doi.org/10.3389/fcimb.2022.1020583.
33. Mima, K., Nishihara, R., Qian, Z.R., Cao, Y., Sukawa, Y., Nowak, J.A., Yang, J., Dou, R., Masugi, Y., Song, M., et al. (2016). *Fusobacterium nucleatum* in colorectal carcinoma tissue and patient prognosis. Gut *65*, 1973–1980. https://doi.org/10.1136/gutjnl-2015-310101.
34. Kunzmann, A.T., Proença, M.A., Jordao, H.W., Jiraskova, K., Schneiderova, M., Levy, M., Liska, V., Buchler, T., Vodickova, L., Vymetalkova, V., et al. (2019). Fusobacterium nucleatum tumor DNA levels are associated with survival in colorectal cancer patients. Eur. J. Clin. Microbiol. Infect. Dis. *38*, 1891–1899. https://doi.org/10.1007/s10096-019-03649-1.
35. Chen, Y., Lu, Y., Ke, Y., and Li, Y. (2019). Prognostic impact of the Fusobacterium nucleatum status in colorectal cancers. Medicine *98*, e17221. https://doi.org/10.1097/MD.0000000000017221.
36. Cremonesi, E., Governa, V., Garzon, J.F.G., Mele, V., Amicarella, F., Muraro, M.G., Trella, E., Galati-Fournier, V., Oertli, D., Däster, S.R., et al. (2018). Gut microbiota modulate T cell trafficking into human colorectal cancer. Gut *67*, 1984–1994. https://doi.org/10.1136/gutjnl-2016-313498.
37. Casasanta, M.A., Yoo, C.C., Udayasuryan, B., Sanders, B.E., Umaña, A., Zhang, Y., Peng, H., Duncan, A.J., Wang, Y., Li, L., et al. (2020). *Fusobacterium nucleatum* host-cell binding and invasion induces IL-8 and CXCL1 secretion that drives colorectal cancer cell migration. Sci. Signal. *13*, eaba9157. https://doi.org/10.1126/scisignal.aba9157.
38. Galeano Niño, J.L., Wu, H., LaCourse, K.D., Kempchinsky, A.G., Baryiames, A., Barber, B., Futran, N., Houlton, J., Sather, C., Sicinska, E., et al. (2022). Effect of the intratumoral microbiota on spatial and cellular heterogeneity in cancer. Nature *611*, 810–817. https://doi.org/10.1038/s41586-022-05435-0.
39. Burn, G.L., Foti, A., Marsman, G., Patel, D.F., and Zychlinsky, A. (2021). The Neutrophil. Immunity *54*, 1377–1391. https://doi.org/10.1016/j.immuni.2021.06.006.
40. Pelka, K., Hofree, M., Chen, J.H., Sarkizova, S., Pirl, J.D., Jorgji, V., Bejnood, A., Dionne, D., Ge, W.H., Xu, K.H., et al. (2021). Spatially organized multicellular immune hubs in human colorectal cancer. Cell *184*, 4734–4752.e20. https://doi.org/10.1016/j.cell.2021.08.003.
41. Mele, V., Basso, C., Governa, V., Glaus Garzon, J.F., Muraro, M.G., Däster, S., Nebiker, C.A., Mechera, R., Bolli, M., Schmidt, A., et al. (2022). Identification of TPM2 and CNN1 as Novel Prognostic Markers in Functionally Characterized Human Colon Cancer-Associated Stromal Cells. Cancers (Basel) *14*, 2024. https://doi.org/10.3390/cancers14082024.
42. Sepich-Poore, G.D., McDonald, D., Kopylova, E., Guccione, C., Zhu, Q., Austin, G., Carpenter, C., Fraraccio, S., Wandro, S., Kosciolek, T., et al. (2024). Robustness of cancer microbiome signals over a broad range of methodological variation. Oncogene *43*, 1127–1148. https://doi.org/10.1038/s41388-024-02974-w.
43. Yipp, B.G., and Kubes, P. (2013). NETosis: how vital is it? Blood *122*, 2784–2794. https://doi.org/10.1182/blood-2013-04-457671.
44. Prince, L.R., Whyte, M.K., Sabroe, I., and Parker, L.C. (2011). The role of TLRs in neutrophil activation. Curr. Opin. Pharmacol. *11*, 397–403. https://doi.org/10.1016/j.coph.2011.06.007.
45. Thomas, C.J., and Schroder, K. (2013). Pattern recognition receptor function in neutrophils. Trends Immunol. *34*, 317–328. https://doi.org/10.1016/j.it.2013.02.008.
46. Duan, S., and Paulson, J.C. (2020). Siglecs as Immune Cell Checkpoints in Disease. Annu. Rev. Immunol. *38*, 365–395. https://doi.org/10.1146/annurev-immunol-102419-035900.
47. Yamanaka, M., Kato, Y., Angata, T., and Narimatsu, H. (2009). Deletion polymorphism of SIGLEC14 and its functional implications. Glycobiology *19*, 841–846. https://doi.org/10.1093/glycob/cwp052.
48. Jaillon, S., Ponzetta, A., Di Mitri, D., Santoni, A., Bonecchi, R., and Mantovani, A. (2020). Neutrophil diversity and plasticity in tumour progression and therapy. Nat. Rev. Cancer *20*, 485–503. https://doi.org/10.1038/s41568-020-0281-y.
49. Schol, P., van Elsas, M.J., Middelburg, J., Nijen Twilhaar, M.K., van Hall, T., van der Sluis, T.C., and van der Burg, S.H. (2024). Myeloid effector cells in cancer. Cancer Cell *42*, 1997–2014. https://doi.org/10.1016/j.ccell.2024.11.002.
50. Wang, X., Fang, Y., Liang, W., Wong, C.C., Qin, H., Gao, Y., Liang, M., Song, L., Zhang, Y., Fan, M., et al. (2024). Fusobacterium nucleatum facilitates anti-PD-1 therapy in microsatellite stable colorectal cancer. Cancer Cell *42*, 1729–1746.e8. https://doi.org/10.1016/j.ccell.2024.08.019.
51. Ren, S.X., Cheng, A.S.L., To, K.F., Tong, J.H.M., Li, M.S., Shen, J., Wong, C.C.M., Zhang, L., Chan, R.L.Y., Wang, X.J., et al. (2012). Host Immune Defense Peptide LL-37 Activates Caspase-Independent Apoptosis and Suppresses Colon Cancer. Cancer Res. *72*, 6512–6523. https://doi.org/10.1158/0008-5472.CAN-12-2359.
52. Lee, H.J., Lee, E.K., Lee, K.J., Hong, S.W., Yoon, Y., and Kim, J.S. (2006). Ectopic expression of neutrophil gelatinase-associated lipocalin suppresses the invasion and liver metastasis of colon cancer cells. Int. J. Cancer *118*, 2490–2497. https://doi.org/10.1002/ijc.21657.
53. Feng, M., Feng, J., Chen, W., Wang, W., Wu, X., Zhang, J., Xu, F., and Lai, M. (2016). Lipocalin2 suppresses metastasis of colorectal cancer by attenuating NF-κB-dependent activation of snail and epithelial mesenchymal transition. Mol. Cancer *15*, 77. https://doi.org/10.1186/s12943-016-0564-9.
54. Weng, M., Yue, Y., Wu, D., Zhou, C., Guo, M., Sun, C., Liao, Q., Sun, M., Zhou, D., and Miao, C. (2022). Increased MPO in Colorectal Cancer Is Associated With High Peripheral Neutrophil Counts and a Poor Prognosis: A TCGA With Propensity Score-Matched Analysis. Front. Oncol. *12*, 940706. https://doi.org/10.3389/fonc.2022.940706.
55. Su, H., Cai, T., Zhang, S., Yan, X., Zhou, L., He, Z., Xue, P., Li, J., Zheng, M., Yang, X., et al. (2021). Identification of hub genes associated with neutrophils infiltration in colorectal cancer. J. Cell. Mol. Med. *25*, 3371–3380. https://doi.org/10.1111/jcmm.16414.
56. Feng, C., Li, Y., Tai, Y., Zhang, W., Wang, H., Lian, S., Jin-si-han, E.E.M.B.K., Liu, Y., Li, X., Chen, Q., et al. (2023). A neutrophil extracellular traps-related classification predicts prognosis and response to immunotherapy in colon cancer. Sci. Rep. *13*, 19297. https://doi.org/10.1038/s41598-023-45558-6.
57. Sheng, W.Y., Yong, Z., Yun, Z., Hong, H., and Hai, L.L. (2015). Toll-like receptor 4 gene polymorphisms and susceptibility to colorectal cancer: a meta-analysis and review. Arch. Med. Sci. *11*, 699–707. https://doi.org/10.5114/aoms.2015.53288.
58. Dang, T.T., Pham, V.N., Tran, N.D., Ngo, T.H., Can, V.M., Nguyen, H.H., Nguyen, T.X., and Dang, T.C. (2025). TLR4/MyD88 expression patterns and novel genetic variants: association with aggressive clinicopathological features in colorectal cancer. Front. Oncol. *15*, 1568729. https://doi.org/10.3389/fonc.2025.1568729.
59. Bindea, G., Mlecnik, B., Tosolini, M., Kirilovsky, A., Waldner, M., Obenauf, A.C., Angell, H., Fredriksen, T., Lafontaine, L., Berger, A., et al. (2013). Spatiotemporal Dynamics of Intratumoral Immune Cells Reveal the Immune Landscape in Human Cancer. Immunity *39*, 782–795. https://doi.org/10.1016/j.immuni.2013.10.003.
60. Peng, D., Kryczek, I., Nagarsheth, N., Zhao, L., Wei, S., Wang, W., Sun, Y., Zhao, E., Vatan, L., Szeliga, W., et al. (2015). Epigenetic silencing of TH1-type chemokines shapes tumour immunity and immunotherapy. Nature *527*, 249–253. https://doi.org/10.1038/nature15520.
61. Nagarsheth, N., Peng, D., Kryczek, I., Wu, K., Li, W., Zhao, E., Zhao, L., Wei, S., Frankel, T., Vatan, L., et al. (2016). PRC2 Epigenetically Silences Th1-Type Chemokines to Suppress Effector T-Cell Trafficking in Colon Cancer. Cancer Res. *76*, 275–282. https://doi.org/10.1158/0008-5472.CAN-15-1938.

62. Barry, S.T., Gabrilovich, D.I., Sansom, O.J., Campbell, A.D., and Morton, J.P. (2023). Therapeutic targeting of tumour myeloid cells. Nat. Rev. Cancer *23*, 216–237. https://doi.org/10.1038/s41568-022-00546-2.

63. Eruslanov, E.B., Singhal, S., and Albelda, S.M. (2017). Mouse versus Human Neutrophils in Cancer: A Major Knowledge Gap. Trends Cancer *3*, 149–160. https://doi.org/10.1016/j.trecan.2016.12.006.

64. Hackert, N.S., Radtke, F.A., Exner, T., Lorenz, H.-M., Müller-Tidow, C., Nigrovic, P.A., Wabnitz, G., and Grieshaber-Bouyer, R. (2023). Human and mouse neutrophils share core transcriptional programs in both homeostatic and inflamed contexts. Nat. Commun. *14*, 8133. https://doi.org/10.1038/s41467-023-43573-9.

65. Pfirschke, C., Engblom, C., Gungabeesoon, J., Lin, Y., Rickelt, S., Zilionis, R., Messemaker, M., Siwicki, M., Gerhard, G.M., Kohl, A., et al. (2020). Tumor-Promoting Ly-6G+ SiglecFhigh Cells Are Mature and Long-Lived Neutrophils. Cell Rep. *32*, 108164. https://doi.org/10.1016/j.celrep.2020.108164.

66. Maser, I.-P., Hoves, S., Bayer, C., Heidkamp, G., Nimmerjahn, F., Eckmann, J., and Ries, C.H. (2020). The Tumor Milieu Promotes Functional Human Tumor-Resident Plasmacytoid Dendritic Cells in Humanized Mouse Models. Front. Immunol. *11*, 2082. https://doi.org/10.3389/fimmu.2020.02082.

67. Zheng, Y., Sefik, E., Astle, J., Karatepe, K., Öz, H.H., Solis, A.G., Jackson, R., Luo, H.R., Bruscia, E.M., Halene, S., et al. (2022). Human neutrophil development and functionality are enabled in a humanized mouse model. Proc. Natl. Acad. Sci. USA *119*, e2121077119. https://doi.org/10.1073/pnas.2121077119.

68. Ali, S.R., Fong, J.J., Carlin, A.F., Busch, T.D., Linden, R., Angata, T., Areschoug, T., Parast, M., Varki, N., Murray, J., et al. (2014). Siglec-5 and Siglec-14 are polymorphic paired receptors that modulate neutrophil and amnion signaling responses to group B *Streptococcus*. J. Exp. Med. *211*, 1231–1242. https://doi.org/10.1084/jem.20131853.

69. Angata, T., Ishii, T., Motegi, T., Oka, R., Taylor, R.E., Soto, P.C., Chang, Y.-C., Secundino, I., Gao, C.-X., Ohtsubo, K., et al. (2013). Loss of Siglec-14 reduces the risk of chronic obstructive pulmonary disease exacerbation. Cell. Mol. Life Sci. *70*, 3199–3210. https://doi.org/10.1007/s00018-013-1311-7.

70. Drewes, J.L., White, J.R., Dejea, C.M., Fathi, P., Iyadorai, T., Vadivelu, J., Roslani, A.C., Wick, E.C., Mongodin, E.F., Loke, M.F., et al. (2017). High-resolution bacterial 16S rRNA gene profile meta-analysis and biofilm status reveal common colorectal cancer consortia. NPJ Biofilms Microbiomes *3*, 34. https://doi.org/10.1038/s41522-017-0040-3.

71. Thomas, A.M., Jesus, E.C., Lopes, A., Aguiar, S., Begnami, M.D., Rocha, R.M., Carpinetti, P.A., Camargo, A.A., Hoffmann, C., Freitas, H.C., et al. (2016). Tissue-Associated Bacterial Alterations in Rectal Carcinoma Patients Revealed by 16S rRNA Community Profiling. Front. Cell. Infect. Microbiol. *6*, 179. https://doi.org/10.3389/fcimb.2016.00179.

72. De Dosso, S., Christoforidis, D., Merlo, E., Vannelli, A., Popeskou, S., Gaffuri, P., Lollo, G., Ambrosiani, L., Radaelli, F., Frattini, M., et al. (2025). Preoperative metronidazole treatment to evaluate its efficacy in reducing Fusobacterium nucleatum colonisation in colorectal cancer patients: a proof-of-concept trial. ESMO Gastrointest. Oncol. *8*, 100169. https://doi.org/10.1016/j.esmogo.2025.100169.

73. Potter, N.S., and Harding, C.V. (2001). Neutrophils Process Exogenous Bacteria Via an Alternate Class I MHC Processing Pathway for Presentation of Peptides to T Lymphocytes. J. Immunol. *167*, 2538–2546. https://doi.org/10.4049/jimmunol.167.5.2538.

74. Beauvillain, C., Delneste, Y., Scotet, M., Peres, A., Gascan, H., Guermonprez, P., Barnaba, V., and Jeannin, P. (2007). Neutrophils efficiently cross-prime naive T cells in vivo. Blood *110*, 2965–2973. https://doi.org/10.1182/blood-2006-12-063826.

75. Giese, M.A., Hind, L.E., and Huttenlocher, A. (2019). Neutrophil plasticity in the tumor microenvironment. Blood *133*, 2159–2167. https://doi.org/10.1182/blood-2018-11-844548.

76. Mele, V., Muraro, M.G., Calabrese, D., Pfaff, D., Amatruda, N., Amicarella, F., Kvinlaug, B., Bocelli-Tyndall, C., Martin, I., Resink, T.J., et al. (2014). Mesenchymal stromal cells induce epithelial-to-mesenchymal transition in human colorectal cancer cells through the expression of surface-bound TGF-β. Int. J. Cancer *134*, 2583–2594. https://doi.org/10.1002/ijc.28598.

77. Hao, Y., Stuart, T., Kowalski, M.H., Choudhary, S., Hoffman, P., Hartman, A., Srivastava, A., Molla, G., Madad, S., Fernandez-Granda, C., et al. (2024). Dictionary learning for integrative, multimodal and scalable single-cell analysis. Nat. Biotechnol. *42*, 293–304. https://doi.org/10.1038/s41587-023-01767-y.

78. Rappsilber, J., Mann, M., and Ishihama, Y. (2007). Protocol for micro-purification, enrichment, pre-fractionation and storage of peptides for proteomics using StageTips. Nat. Protoc. *2*, 1896–1906. https://doi.org/10.1038/nprot.2007.261.

79. Cox, J., and Mann, M. (2008). MaxQuant enables high peptide identification rates, individualized p.p.b.-range mass accuracies and proteome-wide protein quantification. Nat. Biotechnol. *26*, 1367–1372. https://doi.org/10.1038/nbt.1511.

80. Cox, J., Neuhauser, N., Michalski, A., Scheltema, R.A., Olsen, J.V., and Mann, M. (2011). Andromeda: A Peptide Search Engine Integrated into the MaxQuant Environment. J. Proteome Res. *10*, 1794–1805. https://doi.org/10.1021/pr101065j.

81. Cox, J., Hein, M.Y., Luber, C.A., Paron, I., Nagaraj, N., and Mann, M. (2014). Accurate Proteome-wide Label-free Quantification by Delayed Normalization and Maximal Peptide Ratio Extraction, Termed MaxLFQ. Mol. Cell. Proteomics *13*, 2513–2526. https://doi.org/10.1074/mcp.M113.031591.

82. Tyanova, S., Temu, T., Sinitcyn, P., Carlson, A., Hein, M.Y., Geiger, T., Mann, M., and Cox, J. (2016). The Perseus computational platform for comprehensive analysis of (prote)omics data. Nat. Methods *13*, 731–740. https://doi.org/10.1038/nmeth.3901.

83. Gu, Z., Eils, R., and Schlesner, M. (2016). Complex heatmaps reveal patterns and correlations in multidimensional genomic data. Bioinformatics *32*, 2847–2849. https://doi.org/10.1093/bioinformatics/btw313.

84. Davis, M.R., Jr., and Goldberg, J.B. (2012). Purification and visualization of lipopolysaccharide from Gram-negative bacteria by hot aqueous-phenol extraction. J. Vis. Exp. *63*, e3916. https://doi.org/10.3791/3916.

85. Borsig, L., Wong, R., Hynes, R.O., Varki, N.M., and Varki, A. (2002). Synergistic effects of L- and P-selectin in facilitating tumor metastasis can involve non-mucin ligands and implicate leukocytes as enhancers of metastasis. Proc. Natl. Acad. Sci. USA *99*, 2193–2198. https://doi.org/10.1073/pnas.261704098.

86. Uhlen, M., Zhang, C., Lee, S., Sjöstedt, E., Fagerberg, L., Bidkhori, G., Benfeitas, R., Arif, M., Liu, Z., Edfors, F., et al. (2017). A pathology atlas of the human cancer transcriptome. Science *357*, eaan2507. https://doi.org/10.1126/science.aan2507.

87. Liu, J., Lichtenberg, T., Hoadley, K.A., Poisson, L.M., Lazar, A.J., Cherniack, A.D., Kovatich, A.J., Benz, C.C., Levine, D.A., Lee, A.V., et al. (2018). An Integrated TCGA Pan-Cancer Clinical Data Resource to Drive High-Quality Survival Outcome Analytics. Cell *173*, 400–416.e11. https://doi.org/10.1016/j.cell.2018.02.052.

88. Dohlman, A.B., Arguijo Mendoza, D., Ding, S., Gao, M., Dressman, H., Iliev, I.D., Lipkin, S.M., and Shen, X. (2021). The cancer microbiome atlas: a pan-cancer comparative analysis to distinguish tissue-resident microbiota from contaminants. Cell Host Microbe *29*, 281–298.e5. https://doi.org/10.1016/j.chom.2020.12.001.

89. Cerami, E., Gao, J., Dogrusoz, U., Gross, B.E., Sumer, S.O., Aksoy, B.A., Jacobsen, A., Byrne, C.J., Heuer, M.L., Larsson, E., et al. (2012). The cBio cancer genomics portal: an open platform for exploring multidimensional cancer genomics data. Cancer Discov. *2*, 401–404. https://doi.org/10.1158/2159-8290.CD-12-0095.

STAR★METHODS

KEY RESOURCES TABLE

REAGENT or RESOURCE	SOURCE	IDENTIFIER
Antibodies		
Goat polyclonal anti-human IgG-ALP	Sigma-Aldrich	Cat# A-9544; RRID: AB_258459
Leave/Dead viability dye-BV570	Invitrogen	Cat# L34968
Mouse monoclonal anti-CD103-BV605, Ber-ACT8	BD Biosciences	Cat#743652; RRID: AB_2741654
Mouse monoclonal anti-CD11B-APC, ICRF44	BD Biosciences	Cat#746638; RRID: AB_2743917
Mouse monoclonal anti-CD11C-BV650, Ba15	BioLegend	Cat# 337238; RRID: AB_2721552
Mouse monoclonal anti-CD14-BV510, MΦP9	BD Biosciences	Cat#563079; RRID: AB_2737993
Mouse monoclonal anti-CD15-BV750, W6D3	BD Biosciences	Cat# 747426; RRID: AB_2AB_2872112
Mouse monoclonal anti-CD16-BUV615, 3G8	BD Biosciences	Cat#751572; RRID: AB_AB_2875567
Mouse monoclonal anti-CD182-BB700, 6C6	BD Biosciences	Cat# 745876; RRID: AB_AB_2743313
Mouse monoclonal anti-CD19-BUV563, SJ25C1	BD Biosciences	Cat#612917; RRID: AB_2870202
Mouse monoclonal anti-CD1C-PE-CF594, L161	BioLegend	Cat# 331532; RRID: AB_2721552
Mouse monoclonal anti-CD3-APC-Cy7, SK7	BD Biosciences	Cat#561800; RRID: AB_10895381
Mouse monoclonal anti-CD45-BUV805, HI30	BD Biosciences	Cat#612891; RRID: AB_2870179
Mouse monoclonal anti-CD54-BV480, HA58	BD Biosciences	Cat#746638; RRID: AB_2743917
Mouse monoclonal anti-CD66B (purified), unconjugated, G10F5	BD Biosciences	Cat#555723; RRID: AB_396066
Mouse monoclonal anti-CD66B-BB515, G10F5	BD Biosciences	Cat#564679; RRID: AB_2738889
Mouse monoclonal anti-CD89-AF700, A59	BioLegend	Cat#354118; RRID: AB_2750067
Mouse monoclonal anti-CD95-PE/Cy5, DX2	BioLegend	Cat#305610; RRID: AB_314548
Mouse monoclonal anti-CXCR1-BUV395, 5A12	BD Biosciences	Cat#750692; RRID: AB_2874814
Mouse monoclonal anti-EPCAM-PE-Cy7, 9C4	BioLegend	Cat#324221; RRID: AB_2561505
Mouse monoclonal anti-GAPDH, 0411(WB)	Santa Cruz	Cat#sc-47724; RRID: AB_627678
Mouse monoclonal anti-HLA-DR-BUV737, G46-6	BD Biosciences	Cat#748339; RRID: AB_2872758
Mouse monoclonal anti-NKP46-BV785, 9E2	BioLegend	Cat#331945; RRID: AB_2810508
Mouse monoclonal anti-SIGLEC-5/14 (purified), unconjugated, 194128	R&D Systems	Cat#MAB10721; RRID: AB_2738889
Mouse IgG isotype control, unconjugated, 11711	R&D Systems	Cat#MAB002; RRID: AB_ 357344
Rabbit monoclonal anti-SIGLEC-14 (purified), unconjugated, 2457E	R&D Systems	Cat#MAB4905; RRID: AB_ 3658383
Rabbit monoclonal anti-SIGLEC-14-PerCP, 2457E	Novus Biologicals	Cat#FAB4905T
Rabbit monoclonal anti-Syk, EP573Y (WB)	Abcam	Cat# ab40781; RRID: AB_778196
Rabbit polyclonal anti-Phospho-p44/42 MAPK (Erk1/2) (Thr202/Tyr204) (WB)	Cell signaling	Cat#9101; RRID: AB_331646
Rabbit polyclonal anti-p44/42 MAPK (Erk1/2) (WB)	Cell signaling	Cat#9102; RRID: AB_330744
Rabbit polyclonal anti-Phospho-p38 MAPK (Thr180/Tyr182) (WB)	Cell signaling	Cat#9211; RRID: AB_331641
Rabbit polyclonal anti-Phospo Syk (Y323) (WB)	Abcam	Cat# ab63515; RRID: AB_1143194
Rabbit polyclonal anti-p38 MAPK (WB)	Cell signaling	Cat#9212; RRID: AB_330713
Rat monoclonal anti-CCR7-BUV661, 3D12	BD Biosciences	Cat# 741560; RRID: AB_2870987
Rat monoclonal anti-CD115-BV711, 9-4D2-1E4	BD Biosciences	Cat#743144; RRID: AB_2741303
Rat monoclonal anti-CD11B-Pacific Blue, M1/70	BioLegend	Cat#101223; RRID: AB_755985
Rat monoclonal anti-CD16/32-BV661, 190909	BD Biosciences	Cat#750433; RRID: AB_2874596
Rat monoclonal anti-CD18-PE, C71/16	BD Biosciences	Cat#553293; RRID: AB_394762
Rat monoclonal anti-CD54-APC, YN1/1.7.4	BioLegend	Cat#116119; RRID: AB_10613645
Rat monoclonal anti-CD62L-PerCP, MEL-14	BioLegend	Cat#104429; RRID: AB_893397

(*Continued on next page*)

Continued

REAGENT or RESOURCE	SOURCE	IDENTIFIER
Rat monoclonal anti-CX3CR1-BUV496, 2A9-1	BD Biosciences	Cat#750692; RRID: AB_2874814
Rat monoclonal anti-F4/80-BV480, T45-2342	BD Biosciences	Cat# 565635; RRID: AB_2739313
Rat monoclonal anti-Ly-6C-BV605, HK1.4	BD Biosciences	Cat#755205; RRID: AB_3687612
Rat monoclonal anti-Ly-6G-BUV737, 1A8	BD Biosciences	Cat# 741813; RRID: AB_2871151
Recombinant antibody (REAfinity™) anti-SIGLEC-5/14-PE, REA393	Miltenyi Biotec	Cat#130-128-007; RRID: AB_2905383
Secondary anti-Mouse IgM μ-chain HRP Conjugate	Abcam	Cat# ab97230
Secondary anti-rabbit IgG HRP Conjugate	Promega	Cat# W401B
Bacterial and virus strains		
Fusobacterium nucleatum (subsp. Nucleatum, DSM 15643, Fn)	Leibniz Institute DSMZ.	N/A
Bacteroides fragilis (non-enterotoxigenic strain, DSM 2151, Bf)	Leibniz Institute DSMZ.	N/A
Biological samples		
Human Colon Rectal Cancer tissue samples and corresponding adjacent tumor-free tissues	This manuscript	University Basel Hospital, Basel; Ente Ospedaliero Cantonale (EOC), Lugano and Bellinzona, Switzerland;University Basel Hospital, and Klinikum Rechts Der Isar, Münich, Germany
Peripheral Blood Mononuclear Cells from CRC patient and healthy donors	This manuscript	University Basel Hospital, Basel; Ente Ospedaliero Cantonale (EOC), Lugano and Bellinzona
Chemicals, peptides, and recombinant proteins		
Ampicillin sodium salt	Amresco	N/A
Collagenase D	Merck	Cat#11088882001
Dimethyl sulfoxide (DMSO)	Sigma-Aldrich	Cat#D8418
DNase I	Merck	Cat#10104159001
Fetal bovine serum (FBS)	Gibco (Thermo Fisher)	Cat#10270-106
Fluoromount-G™ Mounting Medium	Thermo Fisher Scientific (Invitrogen)	Cat#00-4958-02
GlutaMAX	Gibco (Thermo Fisher)	Cat#35050-061
Growth Factor Reduced Matrigel	Corning Costar	N/A
Hoechst 33342	Thermo Fisher Scientific	Cat#62249
Human serum	Sigma-Aldrich	Cat#H4522
Human Siglec-5-Fc chimera	R&D	Cat#1072-SL
Human Siglec-14-Fc chimera	R&D	Cat#4905-SL
Hyaluronidase type I	Sigma-Aldrich	Cat#H3506
Kanamycin sulfate	Gibco (Thermo Fisher)	Cat#15160-047
Ketamine	Streuli Pharma AG	N/A
Lysozyme	Sigma-Aldrich	Cat#L6876
Paraformaldehyde (PFA)	Sigma-Aldrich	Cat#158127
PEI Prime™ linear polyethylenimine	Sigma-Aldrich	Cat#919012
Phenol (aqueous)	Sigma-Aldrich	N/A
Phosphate-buffered saline (PBS)	Gibco (Thermo Fisher)	Cat#14190-144
PMA (phorbol 12-myristate 13-acetate)	Sigma-Aldrich	Cat#P8139
p-Nitrophenyl phosphate (pNPP)	Sigma-Aldrich	Cat#36199-67-4
Polybrene	Sigma-Aldrich	Cat#H9268
Poly-L-lysine	Sigma-Aldrich	Cat#P8920
Proteinase K (molecular biology grade)	Thermo Scientific	Cat#EO0491
Protein Bloking Buffer	Dako	Cat#X0909

(*Continued on next page*)

Continued

REAGENT or RESOURCE	SOURCE	IDENTIFIER
Puromycin	Sigma-Aldrich	Cat#P8833
RNAsi A	Roche	Cat#10109142001
Reduced Serum Medium	Gibco (Thermo Fisher)	Cat#31985070
RPMI-1640 medium	Gibco (Thermo Fisher)	Cat#42401-018
Triton X-100	Sigma-Aldrich	Cat#X100
Trypsin	Gibco (Thermo Fisher)	Cat#25300-054
Oxoid™ Tryptone Soya Broth	Thermo Fisher	Cat#EB0351w
Vancomycin Hydrochloride	Bio Basic Canada	Cat#VB0983
BBL™ Vitamin K1-Hemin Solution	BD	Cat#212354
TLR2 Inhibitor	BioLegend	Cat#153002
TLR4 Inhibitor, TAK-242, Calbiochem	Sigma-Aldrich	Cat#243984-11-4
Critical commercial assays		
CyQUANT Cell Proliferation Assay Kit	Thermo Fisher Scientific (Invitrogen)	Cat#C7026
EasySep™ Human Neutrophil Isolation Kit	Stem Cell Technologies	Cat#17957
Human CXCL1/GRO alpha DuoSet ELISA	R&D Systems (UK)	Cat#DY275-05
Human CXCL2/GRO beta DuoSet ELISA	R&D Systems (UK)	Cat#DY276-05
Human CXCL5 DuoSet ELISA	R&D Systems (UK)	Cat#DY254-05
Human CXCL8 DuoSet ELISA	R&D Systems (UK)	Cat#DY208-05
LIVE/DEAD™ Fixable Yellow Dead Cell Stain Kit	Thermo Fisher Scientific (Invitrogen)	Cat#L34968
Moloney Murine Leukemia Virus Reverse Transcriptase (M-MLV RT)	Sigma-Aldrich	Cat#M1302-40KU
NucleoSpin RNA Mini Kit for RNA Purification	Macherey-Nagel	Cat#40955.50
Propylene Oxide/Epoxy Resin (Epoxy Embedding Medium Kit)	Sigma-Aldrich	Cat#45359
Pur-A-Lyzer Mega 3500 Dialysis Kit	Sigma-Aldrich	Cat# PURG35010
RNAscope Hydrogen Peroxide	ACDBio	Cat#322335
RNAscope Multiplex Fluorescent Reagent Kit v2	ACDBio	Cat#323110
RNAscope Protease Plus	ACDBio	Cat#322381
RNAscope Target Retrieval Reagent	ACDBio	Cat#322000
SYTOX™ Green Nucleic Acid Stain	Thermo Fisher Scientific	Cat#S7020
TaqMan Universal Master Mix, No AmpErase UNG	Applied Biosystems	Cat#4440040
BD Rhapsody™ cDNA Kit	BD Biosciences	Cat# 633773
BD Rhapsody™ WTA Amplification Kit	BD Biosciences	Cat# 633801
Deposited data		
Raw and analyzed single-cell data	This paper	GEO: GSE311000
Mass spectrometry proteomics data	This paper	ProteomeXchange Consortium,PRIDE: PXD069316
Experimental models: Cell lines		
LS180 Human Colon Cancer cell line	ATCC	Cat#ATCC-CL-187
Luciferase-expressing LS180 (Luc-LS180)	As described in ref. Ali et al.[68]	N/A
DLD-1 (Human Colon Cancer cell line)	ATCC	Cat#ATCC-CCL-221
MC38 (Murin Colon Cancer cell line)	European Collection of Cell Cultures (ECACC)	N/A
CT26 (Murin Colon Cancer cell line)	European Collection of Cell Cultures (ECACC)	N/A
HEK293T (human embryonic kidney cells)	ATCC	CRL-1573; RRID: CVCL_0045
Experimental models: Organisms/strains		
Mice strain: NOD-SCID-gamma (NSG) mice	(NOD.Cg-Prkdcscid Il2rgtm1Wjl/ SzJ Charles River, Germany)	N/A

(*Continued on next page*)

Continued

REAGENT or RESOURCE	SOURCE	IDENTIFIER
Mice strain: NOD-rag-gamma-deficient (NRG) mice	NOD.Cg-Rag1tm1Mom Il2rgtm1Wjl/SzJ, Charles River, Italy)	N/A
Oligonucleotides		
Universal bacterial 16S rRNA gene primers; FW- TCCTACGGGAGGCAGCAGT; RW-GGACTACCAGGGTATCTAATCCTGTT	Microsynth	N/A
Fusobacterium nucleatum 16s rRNA gene primers; FW- GCCTCACAGCTAGGGACAAC; RW-GAGTAAGGGCCGTGTCTCAG	Microsynth	N/A
CXCL1 (human primers): Hs00236937_m1	Applied Biosystems	Cat#4331182
CXCL2 (human primers): Hs00236966_m1	Applied Biosystems	Cat# 4331182
CXCL5 (human primers): Hs00171085_m1	Applied Biosystems	Cat# 4331182
CXL8 (human primers): Hs00174103_m1	Applied Biosystems	Cat# 4331182
CD66b (human primers); FW- 5′-TCAAAGCATTTGCAATCAGC-3′; RW- 5′-GTGGGCAACTTCACAAAGGT-3′	Microsynth	N/A
GAPDH (human primers): Hs02786624_g1	Applied Biosystems	Cat#4331182
SIGLEC-14 (human primers); FW: 5′-AGGATTTATTCTCCCATCTCGCT-3′; RW: 5′-GATGCTGATGGCGAGGTTCTG-3′	Sigma-Aldrich	N/A
SIGLEC-5 (human primers); FW: 5′-GTGGTTCTGACATCTCACCTCATC-3′; RW: 5′-CCTGAAGATGGTGATGGTCTG-3′	Sigma-Aldrich	N/A
Recombinant DNA		
pLenti-C-mGFP-P2A-Puro	Origene	Cat#PS100093
Human SIGLEC5 ORF clone (mGFP-tagged)	Origene	Cat#RC206610L4
Human SIGLEC14 ORF clone (mGFP-tagged)	Origene	Cat#RC224202L4
pCMV-dR8.2	Addgene	Cat #8455
pVSV-G	Addgene	Cat#138479
Software and algorithms		
Adobe Illustrator 27.4	Adobe	RRID: SCR_010279
cBioPortal	https://www.cbioportal.org	N/A
CellSense Microscope Imaging Software	Olympus	N/A
clusterProfiler (v4.6.2)	Bioconductor	RRID:SCR_016884
DoubletFinder (v2.0.6)	GitHub	RRID:SCR_018301
FACS Diva Software	BD Biosciences	RRID: SCR_001456
FACS Symphony A5 Cell Analyzer	BD Biosciences	RRID: SCR_022674
FlowJo v10 + Downsample v3.0.0 + UMAP v2.2 + XShift/Cluster Explorer	FlowJo LLC	RRID: SCR_008520
GraphPad Prism v8.3.1	GraphPad	RRID:SCR_002798
Human Protein Atlas (v23)	https://www.proteinatlas.org	N/A
ImageJ	NIH	RRID:SCR_003070
ImageJ (FiJi)	https://imagej.net/Fiji	RRID:SCR_002285
Leiden algorithm	Seurat / R	N/A
MAPS software	FEI / Thermo Fisher Scientific	N/A
PCA	Seurat / R	RRID:SCR_016341; https://satijalab.org/seurat
R (v4.4.3)	The R Project	RRID:SCR_001905
Seurat (v5.3)	Satija Lab / CRAN	RRID:SCR_016341
Seurat R package v5.1.0	CRAN/Bioconductor	RRID:SCR_016341; https://satijalab.org/seurat

(*Continued on next page*)

Continued

REAGENT or RESOURCE	SOURCE	IDENTIFIER
SoupX (v1.6.2)	GitHub / Bioconductor	RRID:SCR_022543
survival (v3.8-3)	CRAN	RRID:SCR_021065
survminer (v0.4.9)	CRAN	RRID:SCR_021182
TCMA (The Cancer Microbiome Atlas)	https://tcma.pratt.duke.edu/	N/A
UMAP v0.2.10.0	Seurat / R	RRID:SCR_016341; https://satijalab.org/seurat
Other		
Fusobacterium nucleatum -targeted probe for FISH (ATTO488-labeled, 5'-CTA ATG GGA CGC AAA GCT CTC-3')	This paper	N/A

EXPERIMENTAL MODEL AND STUDY PARTICIPANT DETAILS

Clinical specimen collection and processing

Clinical specimens were collected from patients undergoing surgical resection for primary CRC. Cohort 1 included CRC samples and corresponding adjacent tumor-free tissues from patients treated at University Basel Hospital, Basel, and Ente Ospedaliero Cantonale (EOC), Lugano and Bellinzona, Switzerland.

Cohort 2 included only CRC samples from patients treated at University Basel Hospital, and Klinikum Rechts Der Isar, Münich, Germany. Cohorts 3 included CRC samples, corresponding adjacent tumor-free tissues and autologous peripheral blood from patients treated at EOC, Lugano and Bellinzona, Switzerland. Clinicopathological characteristics of patients included in the three cohorts are listed in Tables S1, S2, and S4, respectively.

Informed consent was obtained from all patients. Use of samples and clinical information was approved by local ethical authorities, i.e. Ethikkommission Nordwestund Zentralschweiz (project n. EKNZ 2014-388), Ethics Committee of the School of Medicine of Health of the TUM (project n375/16-S and 2022-169-S-KH), and Comitato Etico Cantonale Ticino (project n. 2020-00437 I CE 3598).

Peripheral blood was used for PBNs isolation (see below). Tumor and adjacent mucosa tissues were snap-frozen for RNA extraction or treated by enzymatic digestion to obtain single-cell suspensions. Briefly, tissues were minced and digested in phosphate-buffered saline (PBS) supplemented with 2 mg/ml collagenase D, 0.2 mg/ml DNAse I, and 0.4 mg/ml hyaluronidase type I for 1 hour on an orbital shaker at 37°C. Single-cell suspensions were then filtered through 70 μm cell strainers and washed twice with PBS supplemented with 2% human serum. They were subsequently used for flow cytometry characterization or preserved at -150°C in human serum with a 10% DMSO final concentration.

Cell lines

Established human (DLD-1, LS180) and murine CRC cell lines (MC38, CT26) were purchased from the European Collection of Cell Cultures and immediately stored in liquid nitrogen. Cells used for individual experiments were thawed from original cryopreserved aliquots and maintained at 37 °C with 5% CO_2 in a humidified incubator, for a maximum of 10 passages, in RPMI 1640 supplemented with 10% fetal bovine serum, 2mM Glutamine and 100 μg/ml kanamycin sulphate. Prior to the investigation, absence of mycoplasma contamination in cell cultures was verified by PCR testing.

LS180 cells and firefly luciferase-expressing LS180 cells (Luc-LS180 cells)[76] were used for *in vivo* experiments.

Animals

All *in vivo* experiments were performed in accordance with institutional and national guidelines and regulations. Experimental protocols were approved by the Commissione cantonale sugli esperimenti su animali (CCEA, project n. R-34752-TI 31/2022/2022). Mice were housed under standard husbandry conditions, including controlled temperature (22 ± 2 °C), humidity (50–60%), a 12 h light/dark cycle, and ad libitum access to food and water and maintained under specific pathogen-free conditions in the BIOS+ Animal Facility.

To assess the impact of gut microbiota on chemokine expression, eight-week-old female mice NOD-SCID-gamma (NSG) mice (NOD.Cg-Prkdcscid Il2rgtm1Wjl/SzJ Charles River, Germany) were injected intra peritoneum (i.p.) or intra cecum (i.c.) with Luc-LS180 cells ($3x10^5$/ mouse), resuspended in a 1:1 mixture of PBS and Growth Factor Reduced Matrigel.

Intracecal injection was performed as previously reported.[36,76] Briefly, mice were anesthetized with ketamine and xylazine i.p. Following laparotomy, cecum was exteriorized, and tumor cells were injected into cecum wall (30 μl / injection). After injection, gut was returned to the abdominal cavity and the incision was closed by atraumatic, resorbable sutures. Following tumor development, starting from day 10, a randomised group of injected mice was treated with Ampicillin sodium salt (1 g/L) and Vancomycin Hydrochloride (0.2 g/L) administered in drinking water. Tumors were harvested on day 30 and assessed for chemokine gene expression.

To evaluate the cytotoxic effect of factors released by bacteria-stimulated neutrophils *in vivo*, eight-week-old female NOD-rag-gamma-deficient (NRG) mice (NOD.Cg-Rag1tm1Mom Il2rgtm1Wjl/SzJ, Charles River, Italy) were injected with Luc-LS180 cells subcutaneously and upon tumor development, approximately at day 6 post-injection, previously collected PBN-bacteria supernatants were injected intratumorally, daily for 10 days. Tumor growth was monitored by bioluminescence and by assessing tumor volumes with a caliper.

Bacteria

Fusobacterium nucleatum (subsp. Nucleatum,DSM 15643, Fn) and *Bacteroides fragilis* (non-enterotoxigenic strain, DSM 2151, Bf) were purchased from the Leibniz Institute DSMZ. Lyophilized cultures were resuspended in filtered Tryptic Soy Broth supplemented with vitamin K and hemin (VWR), and cultured under anaerobic conditions (5% CO2, 0.1% O2, 37°C). First inoculums were diluted in fresh TSB medium and seeded on Schaedler Anaerobe Agar plates during the expansion phase. To obtain growth curves, colony-forming units (CFU) on plates were correlated to the optical density (OD) values of liquid cultures, as assessed by NanoDrop One/OneC spectrophotometer. Frozen stocks of fresh liquid bacterial cultures were prepared in skim milk. For experiments, bacteria cultures were freshly prepared from frozen stocks over a 48-72-hour culture. Bacteria concentration was estimated based on culture OD values.

Neutrophils and bacteria co-cultures

PBNs from healthy donors or CRC patients were isolated by negative sorting with magnetic beads. Purity of isolated cells, as assessed by flow cytometry, was consistently ≥99% (Figure S2). Freshly isolated PBNs were resuspended into phenol red- and serum-free RPMI and plated at a $0.5x10^6$/ml concentration.

They were then cocultured alone or in the presence of live bacteria at a 50:1 bacteria: neutrophil ratio. Neutrophils and their supernatants were collected at different time points (i.e. 1.5, 3, and 6 hours). Neutrophil phenotypes were assessed by large-scale flow cytometry upon staining with specific antibodies (see below). Culture supernatants were centrifuged at high speed and filtered at 0.2 um, to remove potentially residual bacteria, and then tested for cytotoxic activity (see below).

METHOD DETAILS

RNA isolation and Real-time reverse transcription PCR assays

Total RNA was extracted from stored aliquots of CRC tissues or sorted cell populations using Nucleospin RNA kit and reverse transcribed using the Moloney Murine Leukemia Virus Reverse Transcriptase (M-MLV RT). Quantitative Real-Time PCR (qRT-PCR) was performed in the ABI prism™ 7700 sequence detection system, using TaqMan Universal Master Mix, No AmpErase UNG and commercially available primer sequences, as listed in Table S3.

scRNA-seq dataset analysis

ScRNA-seq data from Pelka et al.[40] were retrieved from the GEO series GSE178341. Data relative to cells classified as "Epithelial" isolated from tumoral (n=108131) and non-tumoral tissues (n=60164) were downloaded. Normalization and scaling of raw read counts were performed using the R package Seurat v5.1.0.[77]

Tumor cells and bacteria coculture

Cells from established LS180 and DLD-1 cell lines were incubated with control medium or live Fn or Bf (bacteria: CRC cell ratio = 50:1) at 37°C. After 4 hours, tumor cells were harvested and, following RNA extraction, chemokine gene expression was assessed by quantitative reverse transcription (qRT)-PCR. Alternatively, tumor cells were incubated with bacteria overnight and culture supernatants were collected to perform migration assays (see below) and assess chemokine contents by specific ELISA assays according to the instruction manual.

Migration Assay

Neutrophils isolated from the peripheral blood (PBNs) of healthy donors (see below) were resuspended in serum-free medium, seeded into upper chambers of transwell plates (5 μm pore size, and allowed to migrate towards culture supernatants from tumor cells-bacteria cocultures, at 37°C. After 2 hours inserts were removed and numbers of PBNs migrated into the lower chambers were quantified by CyQUANT Cell Proliferation Assay Kit. In specific experiments, migration assays were performed in the presence of specific chemokine-neutralizing antibodies (10 ug/ml).

Flow cytometry

To assess surface marker expression, cell cultures or single-cell suspensions from tissues were incubated with PBS containing 1% human serum and 2 mM EDTA and stained with fluorochrome-conjugated marker-specific antibodies for 20 minutes at 4°C. Cell viability was determined using the LIVE/DEAD™ Fixable Yellow Dead Cell Stain Kit to exclude non-viable cells from the analysis. Following staining, cells were washed and analyzed using the FACSymphony A5 Cell Analyzer. Data were collected using FACSDiva Software. Compensation controls were set up using single stained compensation beads or cells to correct for spectral overlap. Data analysis was performed using FlowJo software. After compensation matrix adjustment, samples were concatenated

and analyzed using FlowJo plugins (https://flowjo.com/exchange/#/), namely: Downsample (v.3.0.0), UMAP (v2.2), and XShift with Cluster Explorer. UMAP was run using the default settings (Euclidean distance function, nearest neighbors: 15 and minimum distance: 0.5). Antibody used in this study are listed in key resources table.

Western Blot Analysis

Cells were lysed by RIPA buffer containing a protease inhibitor cocktail and phosphatase inhibitor. Lysates were clarified by centrifugation at 14,000 × *g* for 10 min, protein concentration was determined by BCA Protein Assay Kit, and equal protein amounts were mixed with LDS sample buffer and reducing agent and loaded to an 8–12% SDS-polyacrylamide gels for electrophoresis. Following transfer to polyvinylidene difluoride membranes by electroblotting and blocking with 5% (w/v) skim milk in Tris-Buffered Saline with Tween 20 (TBST) for 30 min at room temperature. After that, membranes were incubated overnight with primary antibodies in blocking solution at 4°C. Membranes were then washed and incubated with HRP conjugated secondary antibodies for 1 h at RT. All antibodies are listed in key resources table. Protein was detected by using ECL Western blotting substrate. Antibody used in this study are listed in key resources table.

Proteomic analysis

Culture supernatants from untreated or Fn- or Bf-activated neutrophils were collected after 1.5 and 3 hours and treated as detailed above. Quantitative proteomics analysis was then performed by liquid chromatography–tandem mass spectrometry (LC-MS/MS).

Briefly, for protein extraction and enzymatic digestion, 150 µl of each sample were cleared by centrifugation, flash frozen and stored at -80°C. Proteins were denatured by adding an equal volume of 8M urea, 50 mM ammonium bicarbonate (ABNC, final urea concentration 4M). Proteins were then reduced with 10 mM dithiothreitol for 20 minutes at room temperature and alkylated with 50 mM iodoacetamide for 30 minutes at room temperature. Digestion was carried out in 4M urea supplemented with 1 µg of LysC (1:100 w/w) for 2 hours at room temperature. The digestion buffer was then diluted 1:2 with 50 mM ABC (final concentration 2M urea) and 1 µg of trypsin (1:100 w/w) was added for overnight digestion at room temperature. Digestion was stopped by adding 2% acetonitrile (ACN), 0.3% trifluoroacetic acid (TFA) and the samples were cleared by centrifugation for 5 minutes at maximum speed. Peptides were purified by loading the supernatant into C18 StageTips,[78] and eluted with 80% ACN, 0.5% acetic acid. Finally, the elution buffer was removed by vacuum centrifugation and purified peptides were resolved in 2% ACN, 0.5% acetic acid, 0.1% TFA for single-shot LC-MS/MS measurements.

For LC-MS/MS analysis 1 µg of peptides per sample were separated on an EASY-nLC 1200 HPLC system coupled online via a nanoelectrospray source to a Q Exactive HF mass spectrometer. Peptides were loaded in buffer A (0.1% formic acid buffer) into a 75 µm inner diameter, 50 cm length column in-house packed with ReproSil-Pur C18-AQ 1.9 µm resin (Dr. Maisch HPLC GmbH), and eluted over a 150-min linear gradient of 5 to 30% buffer B (80% ACN, 0.1% formic acid) at a 250 nl/min flow rate. The Q Exactive HF was operated in a data-dependent mode with the Xcalibur software, with a survey scan range of 300-1,650 m/z, resolution of 60,000 at 200 m/z, maximum injection time of 20 ms and AGC target of 3e6.

The top 10 most abundant ions with charge 2-5 were isolated with a 1.8 m/z isolation window and fragmented by higher-energy collisional dissociation (HCD) at a normalized collision energy of 27. MS/MS spectra were acquired with a resolution of 15,000 at 200 m/z, maximum injection time of 55 ms and AGC target of 1e5. Dynamic exclusion was set to 30 s to avoid repeated sequencing.

For LC-MS/MS data analysis, MS raw files were processed using the MaxQuant software v.1.6.7.0.[79] The integrated Andromeda search engine[80] was employed to search spectra against the Human (June 2019), Bf (strain DSM 2151, February 2023), and Fn (strain DSM 15643, February 2023) UniProt databases and a common contaminants database (247 entries), to identify peptides and proteins with a false discovery rate of < 1%. Enzyme specificity was set as ''Trypsin/P'' with a maximum of 2 missed cleavages and a minimum length of 7 amino acids. N-terminal protein acetylation and methionine oxidation were set as variable modifications, and cysteine carbamidomethylation as a fixed modification. Match between runs was used to transfer identifications across samples based on mass and normalized retention times, with a matching time window of 0.7 min and an alignment time window of 20 min.

Label-free protein quantification (LFQ) was performed with the MaxLFQ algorithm[81] with a minimum required peptide ratio count of 1. Data analysis was performed using the Perseus software v.1.6.2.3.[82] Data were filtered by removing proteins only identified by site, reverse hits, and potential contaminants and only human proteins were kept for subsequent analysis. After log2 transformation of LFQ intensities, four biological replicates from both the same and different donors were grouped and a filter for a minimum of 70% valid values in at least one group was applied.

For statistical analysis, missing data points were replaced by imputation from a normal distribution with 0.3 width and 1.8 downshift, and an ANOVA multiple-sample test (0.05 permutation-based FDR, 250 randomizations) was used to identify significant protein intensity changes across the experimental groups. Differentially expressed proteins were visualized by Z-scoring with the R package ComplexHeatmap v2.14[83] and are listed in Table S6. Hierarchical clustering (complete) of ANOVA-significant protein intensities and samples was also performed.

Transmission Electron Microscopy

Cells pellets were fixed with 2,5% glutaraldehyde in 0,1M cacodylate buffer (pH 7.4) for 1 hour at room temperature. After several washes in cacodylate buffer, samples were post-fixed in reduced osmium solution (1% OsO4, 1,% potassium ferrocyanide in 0,1M cacodylate buffer, pH 7.4) for 2 hours on ice. Following multiple washes in Milli-Q water, sections were incubated in 0,5%uranyl acetate overnight at 4°C. Samples were then dehydrated with increasing concentration of ethanol, rinsed in propylene oxide an

infiltrated overnight at room temperature in a mixture of propylene oxide/epoxy resin (Epoxy Embedding Medium kit). There were embedded in pure resin and baked at 60°C for 48hours. Ultrathin sections were cut using an ultramicrotome (UC7, Leica microsystem, Vienna, Austria), collected on copper grids stained with uranyl acetate and Sato's lead solutions. Sections were examined on a Transmission Electron Microscope Talos L120C (FEI, Thermo Fisher Scientific) operating at 120kV and images were acquired using Velox software.

Correlative Light Electron Microscopy (CLEM) on FFPE tissue sections

After confocal imaging the glass slide were soaked in PBS and the glass coverslips were carefully removed. Sections were fixed with 2,5% glutaraldehyde in 0,1M cacodylate buffer for 1h at RT. After several rinses in 0,1M cacodylate buffer, samples were postfixed using the ROTO technique consisting in treatments for 90 minutes on ice in reduced osmium solution (1% OsO4, 1,5% potassium ferrocyanide in 0,1M cacodylate buffer pH 7.4), 20 minutes at RT in thiocarbohydrazide (1% in water) and for 30 minutes at RT in osmium tetroxide (2% in water). After several washes in milliQ water sample were en-bloc stained overnight at 4°C in 0,5% uranyl acetate. Samples were then dehydrated with increasing concentration of ethanol embedded in epoxy resin and polymerized overnight at 45C° and 24 hours at 60C°. Resin blocks were detached from glass slides using liquid nitrogen. Thin sections (70-90 nm) were collected using an ultramicrotome (UC7, Leica microsystem, Vienna, Austria) and deposited on copper carbon-coated slot grids. Grids were contrasted with uranyl acetate and Sato's lead solution and imaged using a TALOS L120C transmission electron microscope. Confocal images were imported in MAPS software and DAPI staining were used as a reference in order to relocate the same region in ultrathin sections. Large view fields were acquired by tile image acquisition and stitched using MAPS software.

Confocal and EM images were then aligned using the ec-CLEM plugin in Icy software.

Cytotoxic activity of culture supernatants

LS180 cells were seeded in triplicate in 24-well plates at a density of $3.5x10^5$ cells/well in 1ml RPMI 1640 medium. On the following day, culture medium was removed, and cells were treated with 0.25 ml of fresh medium (control), or culture supernatant derived from bacteria-stimulated PBNs cocultures. Following a 24-hour treatment period, cells were harvested and stained with Live/Dead, and sequentially incubated with Annexin V, according to the manufacturer's protocol. Percentages of dead CRC cells was determined by flow cytometry and calculated as the sum of the proportions of Annexin V^+ and Annexin V^+Live/$Dead^+$ cells. Statistical significance of differential cell death rates was assessed by Friedman test.

Siglec-5/14 Genotyping

Genotyping of Siglec-5 and-14, was performed as previously reported.[47]

SIGLEC-5 and *SIGLEC-14* and were amplified by using specific primer pairs, i.e. 5FW + 5RW and 14FW + 14RW, respectively (see key resources table). *SIGLEC-5/14* fusion gene was amplified by using 14FW + 5RW pair. Each reaction tube contained the following (in 20 μl): genomic DNA, 100 ng; primers, 0.3 μM each; dNTP, 0.2 mM each; Expand High Fidelity enzyme (Roche Diagnostics, Basel, Switzerland), 0.49 U; in 1 Å~ PCR plus MgCl2 buffer (Roche). Thermal cycling parameters were as follows: 94°C, 2 min; (94°C, 15 s; 56°C, 30 s; 72°C, 1.5 min) Å~ 10 cycles; (94°C, 15 s; 56°C, 30 s; 72°C, 1.5 min + 5 s/cycle) Å~ 20 cycles; 72°C, 7 min.

LPS purification

LPS from *F. nucleatum* was purified using the hot aqueous-phenol method as described.[84] Briefly, bacteria were harvested from a 1 L culture at OD_{600} 1.8, pelleted by centrifugation at 10,000 x g for 10 min, washed with 40 mL of ice-cold water and pelleted again. Cell pellets were resuspended in 20 mL of 2% SDS, 10% glycerol, 2% β-ME in 50 mM Tris-HCl, pH 6.8, boiled at 95°C for 30 min and froze down. Samples were then incubated twice with DNase I and RNase A at a final concentration of 50 μg/mL, 37°C for 30 min, followed by a subsequent proteinase K treatment at a final concentration of 50 μg/mL at 55°C overnight. Equal volumes of phenol were added to the samples, thoroughly mixed and incubated for 15 min at 65°C. For the extraction, after the addition of diethyl ether (150 ml) to the samples, vortexing for 30 s and centrifuged at 13,000 x g for 20 min. The upper phase was discarded, and phenol extraction was repeated. For precipitation, samples were supplemented with 0.5 M sodium acetate, along with 10-times the volume of 95% ethanol and stored overnight at -20°C. Samples were centrifuged at 3,000 x g at 4°C for 10 min, and the pellet was resuspended in 20 mL deionized water and dialyzed using the Pur-A-Lyzer Mega 3500 Dialysis Kit and lyophilized. Phenol extractions and dialysis were repeated, and final products were stored at -20°C.

ELISA analysis of bacterial LPS

Bacterial LPS was resuspended in methanol and ELISA plates were coated by evaporating the methanol.[85] The wells were washed with HBSS and blocked with 0.5% BSA in HBSS for 1 h at RT. Human-Siglec-5 and Siglec-14-Fc chimera at concentration of 1ug/mL were pre-complexed with goat-anti-human IgG Ab conjugated with alkaline phosphatase at 1:100 for 1 h at RT. Pre-complexed chimeras were then incubated with LPS for 2 h at RT. The wells were washed with 0.5% BSA in HBSS followed by three washes with HBSS. After a final wash, the p-nitrophenyl phosphate substrate was added and allowed to develop for 1-5 min at RT, and absorbance was measured at 405 nm.

PEI-mediated transfection and lentiviral infection

The HEK293T cells were transfected with a vector for each overexpression plasmid, packaging, and envelope vector using the PolyEthylenImine (PEI) method. The HEK293T cells were seeded in a 100mm culture dish (4x10^{6}cells/plate) and incubated overnight at 37 C in a 5% CO2-humidified atmosphere. After 24 h, the vector plasmid (3 μg), packaging plasmid (pCMV-dR8.2; 2.7 μg), and envelope plasmid (pVSV-G; 0.7 μg) were mixed in Opti-MEM I Reduced Serum Medium (300 μL/10 cm culture dish; Cat 31985070, Gibco) and with 1.25 mM PEI (Sigma-Aldrich 919012) solution (ratio μL PEI: μg DNA 4:1). The DNA/PEI mixture were incubated for 15 min at room temperature and added to the HEK 293T cell supernatant. After 48 h of transfection, the viral supernatants were collected and filtered through a 0.45μm filter. The THP1 cell line is then incubated with the viral supernatant and 8 μg/ml Polybrene (for 72h and then selected with 5 μg/mL puromycin for one week.

Plasmids

The pLenti-C-mGFP-P2A-Puro, Lenti vector with C-terminal mGFP tag and P2A-Puro the Lenti ORF clone of Human sialic acid binding Ig-like lectin 5 (SIGLEC5), mGFP tagged, and the Lenti ORF clone of Human sialic acid binding Ig-like lectin 14 (SIGLEC14), mGFP tagged were purchased from Origene.

Immunofluorescence microscopy

PBNs, isolated as described above, were seeded at 0.5*10^6 cell/well into 24 wells with poly-L-lysine coated glass circle slides (12mm diameter) and rested at 37°C, in 5% CO2, for 30 minutes. Fn or Bf ware then added (bacteria: neutrophil ratio 50:1), and slides were incubated at 37°C, in 5% CO2, for 5, 30, and 90 minutes. To visualize bacteria attachment to cell surface, in specific experiments slides were kept on ice, thus preventing bacteria internalization. DID-fluorescence was used to visualize bacteria internalization into PMN. Following PBS washes, cells were fixed with 1% PFA diluted in PBS for 10 minutes at room temperature. Cells were permeabilized with 0.3% Triton X-100 in PBS for 15 minutes and blocked with PBS 2% FBS. Nuclei were stained with Hoescht 33342 (1 μg/mL) and coverslips were mounted over slides in Fluoromount-G™ mounting medium. Images were captured using a confocal laser-scanning fluorescence microscope Leica SP5 (Molecular Probes, Leica Microsystem, Manheim, Germany). For qualitative and quantitative analyses, the ImageJ software with the Fiji plugin was used (Rasband, W·S, ImageJ, U.S. National Institute of Health, Bethesda, Maryland, USA). A Leica TCS SP5 microscope (Leica Microsystems) with a Leica HCX PL APO lambda blue 63.0 × 1.40 OIL UV objective was used to acquire confocal images. The acquisition software Leica LAS X was used. Image processing was performed with Fiji/ImageJ and Imaris software 460 (Oxford Instruments, v9.9.1).

For Siglec-5/14-Fn colocalization, three-dimensional images were acquired using an HCX PL APO Lambda Blue ×63.0 1.40 numerical aperture oil-immersion objective. Three-dimensional cell surface reconstruction was performed using Imaris software.

Live imaging

A chambered coverslip (μ-Slide 8 Well High Glass Bottom, Ibidi),were coated with 0.01% (m/v) poly-L-lysine solution upon incubation in dH2O at room temperature for 30 minutes. PBNs, isolated as described above were seeded at 0.5x106 cells/well and incubated at 37°C in 5% CO2. After a 30 minute-incubation at 37°C in 5% CO2, PBNs were washed with RPMI without Phenol Red and stained with Hoescht 33342 (1 μg/mL) Sytox Green (1μg/ml) in complete RPMI without Phenol Red for 10 min at 37°C with 5% CO2. Cells were treated with Fn or Bf (bacteria: neutrophil ratio 50:1), or PMA (100nM), and incubated at 37°C, in 5% CO2, for 6 hours. Time-lapse video microscopy was conducted every 5 minutes for 3 hours using an ImageXpress® (Molecular Devices) high throughput microscope, equipped with an incubation system, at 20x magnification.

RNAscope

RNAscope staining was performed on 4-μm sections of formalin-fixed paraffin-embedded (FFPE) CRC tissues using RNAscope Multiplex Fluorescent Reagent Kit v2 Assay, according to the manufacturer's protocol with minor adaptations.

Deparaffinization was achieved upon sequential incubation in OTTIX Plus (Diapath, X0076; 2x 5 minutes) and in OTTIX Shaper (Diapath, X0096; 1x 5 minutes). Afterwards, sections were incubated in RNAscope Hydrogen Peroxide for 10 min at RT, then in RNAscope Target retrieval reagent for 45 minutes and finally in RNAscope Protease Plus for 30 min at 40 °C.

To permeabilize bacteria Gram+ envelopes, samples were then treated with lysozyme 10 mg/ml for 90 min at 40°C, prior to incubation with a mix of probes specific for Fn (RNAscope™ Probe- B-Fusobacterium-23S-3zz-C3), or pan-16SrRNA (RNAscope™ Probe- EB-16S-rRNA-C2), for 2h at 40°C. Signal amplification and development were carried out using RNAscope Multiplex Fluorescent Reagent Kit v2 Assay, according to the instruction manual. As fluorophores, TSA Vivid 570 (1:1500) for pan-16SrRNA-specific, and TSA Vivid 650 (1:1000) for Fn-specific probe were used.

Images were captured using a confocal laser-scanning fluorescence microscope Leica SP5 (Molecular Probes, Leica Microsystem, Mannheim, Germany). For qualitative analyses, the ImageJ software with the Fiji plugin was used (Rasband, W·S, ImageJ, U.S. National Institute of Health, Bethesda, Maryland, USA). A Leica TCS SP5 microscope (Leica Microsystems) was used to acquire confocal images at 40x magnification.

Immunohistochemistry

Four-μm-sections of FFPE CRC tissues were deparaffinized upon sequential incubation in OTTIX (2x 5 minutes) and in OTTIX Shaper (Diapath, X0096; 1x 5 minutes). Antigen retrieval was performed upon incubation in a pH 6 solution at 98°C for 20 minutes.

Subsequently, samples were incubated in 3% H_2O_2 for 10 minutes, to block endogenous peroxidases, and in Protein-Block solution to prevent non-specific binding. Sections were then stained for anti-Cleaved Caspase 3 antibodies (1:2000) and CD66b (1:100) antibodies developed with DAP Peroxidase (HRP) substrate. Slides were acquired with an Aperio AT2 Slide scanner using Imagescope software (Leica Biosystems). Antibody used in this study are listed in key resources table.

Rhapsody

Six samples were processed in this experiment using the BD Rhapsody™ single-cell RNA-seq workflow. The number of cells recovered per sample was from approximately $2x10^6$. Reverse transcription was performed on mRNA captured by BD Rhapsody™ Cell Capture Beads using the BD Rhapsody™ cDNA Kit, following the manufacturer's instructions. This step generated bead-bound cDNA via oligo(dT)-primed reverse transcription. Whole transcriptome amplification (WTA) was then carried out using the BD Rhapsody™ WTA Amplification Kit, which amplifies 3′ end transcript fragments through targeted PCR to produce whole-transcriptome libraries. Purification steps were conducted using SPRIselect magnetic beads according to the recommended ratios for each step of the protocol. Final libraries were quantified using the Qubit™ dsDNA High Sensitivity Assay Kit (Thermo Fisher Scientific), and size distribution was assessed on an Agilent 2100 Bioanalyzer using the High Sensitivity DNA kit (Agilent Technologies). The resulting libraries were sequenced on an Illumina NextSeq 2000 system using 100-cycle kits, with read configuration 51–8–8–71 (Read1–i7–i5–Read2).

Samples were distributed across two separate runs on P4 flow cells to ensure sufficient sequencing depth. Final libraries were stored at −20 °C prior to pooling and sequencing.

BD Rhapsody™ Whole Transcriptome Analysis (WTA)

Raw FASTQ data were processed using the BD Rhapsody™ Sequence Analysis Pipeline (v2.2.1), with the pre-built RhapRef_Human_WTA_2025-03 reference. All parameters were left at their default settings. Single cell RNA-seq data analysis was conducted with the R package Seurat (v5.3), and with R version 4.4.3. For each sample, ambient RNA contamination was corrected using SoupX (v1.6.2) after initial clustering with SCTransform, PCA, UMAP, and graph-based clustering. Cells with fewer than 200 detected genes or more than 10% mitochondrial transcript content were excluded. Doublets were identified and removed with DoubletFinder (v2.0.6) by estimating expected doublet rates from BD Rhapsody specifications and correcting for homotypic doublets. After quality control, single-cell objects from individual donors were merged into a single Seurat object, with metadata annotations for donor genotype (wild-type or null) and treatment condition (neutrophils-Fn, neutrophils-Bf, or normal neutrophils), and resulted in a total of 157248 cells. Data were normalized, highly variable genes identified, scaled, and reduced by PCA. Clustering was performed using the Leiden algorithm (resolution = 0.05), and UMAP was used for visualization. Differential expression analysis was performed with Seurat's Wilcoxon test, considering genes with adjusted $p \leq 0.05$ and $|log2FC| \geq 0.25$ as significant. Functional enrichment analysis was conducted with the R package clusterProfiler (v4.6.2) using GO biological process and KEGG pathways.

TMA construction

The TMA used in this work was constructed by using >500 non-consecutive, formalin-fixed and paraffin-embedded primary CRC samples, from the tissue biobank of the Institute of Pathology of the University Hospital Basel (Switzerland), as previously described.[13,14,16] A semi-automated tissue arrayer was used to transfer 0.6 mm diameter punches from tissue blocks onto glass slides. Punches were derived from tumor centers and consisted of at least 50% tumor cells. Clinical-pathological data of patients included in the TMA are summarized in Table S7. Use of clinical information was approved by local ethical authorities.

Fn detection in CRC TMA by FISH

FISH assay was performed as previously reported.[36] Five-μm TMA sections were fixed with 4% PFA for 20 min on ice followed by a washing step in PBS. Slides were then dipped into ice-cold methanol prior to hybridization with a Fn-targeted probe (ATTO488-labeled, 5'-CTA ATG GGA CGC AAA GCT CTC-3') in hybridization buffer (20mM Tris-HCL; 0.9% NaCl; 0.1% SDS) at 48°C for 16h. Subsequently, slides were washed twice in hybridization wash buffer (20mM Tris-HCL; 0.9% NaCl; pH 7.2) for 30 min at 48°C, dipped in PBS, mounted with ProLong Gold Antifade Mountant with DAPI and evaluated with a fluorescence microscopy (Bx43 Olympus). Images were analyzed using CellSense software (Olympus) and ImageJ (FiJi).

Survival analyses in TMA

CD66b staining was performed as previously described.[16] Patients were stratified as $CD66b^{high}$ versus $CD66b^{low}$ using an optimal cut-off value of 8 cells per punch. Stratification as Fn-high versus Fn-absent/low was based on numbers of Fn-positive spots detected per punch. Tumor were considered Fn-high when >=30 spots per punch and/or presence of large aggregates were detected. After dichotomization, Kaplan–Meier curves were plotted, and compared by log-rank test. Cox proportional hazards regression models from the R package 'survival' (v3.8-3) were fitted to account for MSI status, patient age, and tumor grade. Forest plots were generated using the 'survminer' (v0.4.9) package to display covariate-adjusted p-values and HRs.

Survival Analysis in TCGA

Expression data of *CXCL1*, *CXCL2*, *CXCL5*, *CXCL8*, and *CEACAM8* genes from COAD and READ TCGA cohorts, were retrieved from the Human Protein Atlas.[86] Survival data for TCGA samples were retrieved from Liu et al..[87]

For each gene, patients were dichotomized in "high" and "low" expression groups based on the optimal FPKM expression cut-off, i.e. the FPKM value of each gene that yields maximal difference with regard to survival between the two groups at the lowest log-rank P-value (CXCL1: cut-off=35.05; CXCL2: cut-off=7.41; CXCL5: cut-off=0.72; CXCL8: cut-off=17.39; CEACAM8: cut-off= 0.036). Overall survival was defined as the time from diagnosis to death from any cause or to the date of last follow-up, with patients alive at last follow-up censored.

Relative Fn abundance was evaluated from The Cancer Microbiome Atlas (TCMA)[88] website (https://tcma.pratt.duke.edu/) by downloading data from the COAD and READ cohorts and selecting genus as the taxonomic level. This filtering yielded 170 samples which were then stratified into Fn-high versus Fn-absent/low based on median relative abundance.

Overall survival analysis was performed using Kaplan-Meier estimates and log-rank testing to compare the following groups: Fn-high versus Fn-absent/low, and Fn-high/CEACAM8-high or Fn-absent/low/CEACAM8-high versus CEACAM8-low. Hazard ratios (HRs) and corresponding 95% confidence intervals (CIs) were estimated using Cox proportional hazards regression models.

Normalized mRNA expression values (RNA Seq V2) of *SIGLEC14* and *SIGLEC5* in the COAD-READ TCGA cohort (TCGA, Firehose Legacy, n=382), were retrieved from cBioPortal.[89] Patients were stratified in two groups: SIGLEC14-NE, characterized by absent *SIGLEC14* expression (=0; n=31), and SIGLEC14-E, characterized by detectable *SIGLEC14* expression (>0; n=351). Overall survival in the two patient groups was compared using Kaplan-Meier estimates and log-rank testing. *SIGLEC5* and *CEACAM8* expression levels in SIGLEC14-NE and SIGLEC14-E groups were comparatively evaluated using a two-sided Wilcoxon rank-sum test.

Survival analyses were performed using the R package survminer v0.4.9.

QUANTIFICATION STATISTICAL ANALYSIS

Statistical analyses were performed in R with RStudio, or in GraphPad Prism (GraphPad Prism 9.0 software). Microscopy images were analyzed with Fiji/ImageJ and Imaris for qualitative and quantitative assessments, including 3D reconstructions and colocalization. Immunohistochemistry and FISH were quantified using ImageScope, CellSense, and Fiji. Tumors were stratified as CD66b high/low or Fn high/low based on predefined cut-offs. Survival analyses (Kaplan–Meier and log-rank test) were performed using the R package survminer (v0.4.9). Statistical analyses of quantitative experimental models were performed using the Mann-Whitney test for group comparisons, one-way or two-way ANOVA for multiple comparisons, as appropriate. In vitro experiments were carried out with at least three independent biological experiments or as indicated by N in the figure legends. Data are represented as mean ± SD with the level of significance defined as $p < 0.05$, unless otherwise specified. Figure asterisks correlate to p-value: * $p \leq 0.05$, ** $p \leq 0.01$, *** $p \leq 0.001$, **** = p 0.0001, ns=not significant; unless otherwise specified.